# Investigation of Fluorescence Coherence Tomography for Optofluidic Applications

**by**

**Lukas-Karim Merhi**

B. A. Sc., Simon Fraser University, 2011

Thesis Submitted in Partial Fulfillment of the
Requirements for the Degree of
Master of Applied Science

in the
School of Engineering Science
Faculty of Applied Science



**SIMON FRASER UNIVERSITY**

**Spring 2014**

# Approval

**Name:** **Lukas-Karim Merhi**

**Degree:** **Master of Applied Science**

**Title of Thesis:** ***Investigation of Fluorescence Coherence Tomography for Optofluidic Applications***

**Examining Committee:**

**Dr. Mirza Faisal Beg, P. Eng.**
Chair
Associate Professor

_____

**Dr. Marinko V. Sarunic, P. Eng.**
Senior Supervisor
Associate Professor

_____

**Dr. Glenn Chapman , P. Eng.**
Supervisor
Professor

_____

**Dr. Ash Parameswaran, P. Eng.**
Internal Examiner
Professor
School of Engineering Science

_____

**Date Defended/Approved:** February 28, 2014

## Partial Copyright Licence

## Abstract

Conventional Flow Cytometers (FC) and Fluorescence-Activated-Cell-Sorters (FACS) are mechanically complex, bulky, and require specialized human operators, large sample volumes, and sample preparation procedures for proper diagnosis of diseases such as leukemia and malaria. For this reason, there has been an increasing demand for miniaturization, reduction of cost, and portability of such devices. Lab-on-a-chip devices, which integrate microfluidics with other technologies, have been emerging as a potential solution to miniaturization of FC/FACS technology. One serious limitation of lab-on-a-chip devices is their inability to extract shape or morphological information which is very useful for cell differentiation and characterization. To meet this challenge, optical imaging techniques and microfluidics are combined to form a subset field in 'optofluidics'. This thesis will help explore this field which describes systems that combine optics and microfluidics.

In this thesis, as proof of principle, the integration of a novel optical imaging technique called Fluorescence Coherence Tomography (FCT) with microfluidics is presented. The FCT was used to measure the position of flowing fluorescent particles in the cross section of the microfluidic channel (perpendicular to the direction of flow). This type of measurement was motivated by recent reports in the literature demonstrating that a cell's position in a microchannel is highly sensitive to its size and stiffness, which in turn are important biomarkers for cell classification. By combining FCT with microfluidics, the long term goal is to provide researchers and scientists with new possibilities for biological investigations in optofluidic applications. The preliminary results acquired through this work are important for future development of applications in the miniaturization of molecule specific flow cytometry.



**Keywords**: fluorescence, fluorescence coherence tomography, optical coherence tomography, optofluidics, microfluidics

## Acknowledgements

I would like to express my deepest gratitude to my senior supervisor, Dr. Marinko V. Sarunic. He has been an exceptional mentor over the last three years both in this research and outside of work. His continuous support and patience has been instrumental in completing my degree. He also provided me with opportunities to work with collaborators in Montreal, encouraged me to travel to India and establish new research connections there. These experiences have had a huge impact in my personal growth. I have become a much better engineer, scientist, and researcher due to his guidance.

I would like to thank Dr. H. Uri Saragovi, Dr. Glenn Chapman, Dr. Mirza Faisal Beg, Dr. Ash Parameswaran, Dr. Andrew Rawicz, Dr. Soumyo Mukherji, Dr. Sae-won Lee, Dr. Eric Lin, and Dr. Ajit Kholsa for playing a supervisory role throughout my Masters degree. They provided me with knowledge and support essential for the completion of my degree and insights that enriched my graduate experience.

I would like to thank many members of the School of Engineering Science and the SFU community: Andras Szigeti, Hsiu-Yang Tseng (Steven), Gary Houghton, Raj Pabla, and Lindsay Ward for their time, interest in my project, and support throughout my graduate degree.

I would like to thank Dr. Thomas Abraham and Dr. Pierre Lane for their advice and support during my graduate degree.

I would like to thank Bhuvaneshwari Karunakaran (Bhuvana) for being a great host during my time in India and being a great research partner during the last phase of my degree. She was instrumental to the completion of this research.

I am very fortunate and honored to have been part of the Biomedical Optics Research Group (BORG). I am especially appreciative to Michelle Cua, Yifan Jian, Jing Xu, Kevin Wong, and past members of BORG Mei Young, Ali Issaei, Lukasz Szczygiel, and Nima Javaheri. I could not have asked for greater colleagues and friends.

Lastly, I would like to thank my family for their love, support, and curiosity during my graduate endeavor.

# Table of Contents

# List of Tables

# List of Figures

# List of Symbols

| | |
|---|---|
| $I(k)$ | intensity as a function of wavenumber |
| $\hat{I}(z)$ | Fourier transform of $I(k)$ |
| $k$ | wavenumber |
| $l_c$ | coherence length |
| $z_{max}$ | maximum possible observable $\Delta z$ for the system |
| $\Delta z$ | physical path length difference |
| $\lambda$ | wavelength |
| $S(k)$ | spectral density function |
| $\hat{S}(z)$ | Fourier transform of $S(k)$ |
| $E_R$ | electric field for reflected fluorescence |
| $E_S$ | electric field for direct fluorescence |
| $\delta(z \pm \Delta z)$ | delta functions |
| $\mu$ | peak value |
| $\sigma$ | standard deviation of the noise floor |
| $w$ | incident laser beam waist |
| $w_0$ | laser beam wait |
| $\theta_i$ | incident angle |
| $\theta_m$ | diffracted angle |
| $y$ | linear dispersion |
| $D$ | angular dispersion |
| $\Delta\lambda_{\min}$ | minimum resolvable wavelength |
| $Z_R$ | Rayleigh range |

# Glossary

| | |
|---|---|
| OCT | Optical Coherence Tomography |
| FCT | Fluorescence Coherence Tomography |
| FD OCT | Fourier Domain Optical Coherence Tomography |
| FLIC | FLuorescence Interference Contrast |
| SSFM | Spectral Self-Interference Fluorescence Microscopy |
| SD FCT | Spectral Domain Fluorescence Coherence Tomography |
| SDFCPM | Spectral Domain Fluorescence Coherence Phase Microscopy |
| CCD | Charged-Couple Device |
| SNR | Signal to Noise Ratio |
| ND: YAG | Neodymium-doped Yttrium Aluminium Garnet |
| PDMS | Polydimethylsiloxane |
| SU-8 | Permanent epoxy negative photoresist |
| LCI | Low-Coherence Interferometry |

# Chapter 1. Introduction

## 1.1. Overview

Screening blood samples is an important step in the diagnosis of diseases, such as leukemia[1] and malaria[2], [3]. Sophisticated equipment such as Flow Cytometers (FCs) and Fluorescence-Activated-Cell-Sorters (FACS) is used for the detection and classifications of cells. FCs and FACS operate based on the observation that different particles scatter light in characteristic patterns and emit fluorescence that both of which are potentially distinct, permitting identification of different types of cells.

Conventional FCs and FACS are mechanically complex, bulky, and require specialized human operators, large sample volumes, and sample preparation procedures for proper disease diagnostics. Consequently, there has been an increasing demand for miniaturization, lower cost and portability of such devices for point-of-care applications, especially for the detection of malaria and leukemia through whole blood analysis [4]–[9]. A potential solution to miniaturization of FC/FACS technology has recently been emerging Lab-on-a-chip devices, which integrate microfluidics with other technologies (e.g. acoustic, magnetic, electrical, electrochemical, and mass spectrometry mechanisms) [10], [11]. Microfluidics is effective because it can manipulate fluids which are often the type of samples used in disease diagnostics such as blood. One of the biggest limitations of lab-on-a-chip devices is their inability to extract shape or morphological information which is often the first characteristic used for cell differentiation and characterization [12]–[15]. To meet this challenge, optical imaging techniques and microfluidics are combined forming a subset field in ‘optofluidics’ [11], [16], [17]. This thesis will help explore this field which describes systems that combine optics and microfluidics [8], [17]. The strength of applying optical imaging techniques to microfluidics is that it can obtain shape or morphological information within biological samples through a non-contact and non-ionizing acquisition method and potentially

provide molecular contrast [16]. Examples of molecular specific contrast used in optofluidics include fluorescence, surface enhanced Raman spectroscopy, surface enhanced Plasmon resonance, hyper-spectral imaging, and many more [11].

The long term goal of this thesis is to provide researchers and scientists with a new optofluidic (lab-on-chip) device for biological investigations. To accomplish this, the objective of this thesis is to investigate the integration of a novel optical imaging technique called Fluorescence Coherence Tomography (FCT) with microfluidics in order to localize particles within a microfluidic channel. In the next paragraphs, the rationale behind the development of FCT for microfluidic devices is presented.

## 1.2. Background

Light incident on a tissue can be transmitted, reflected, absorbed, or scattered. The scattering of light can be detrimental to imaging because scattered photons hide or obscure important information, deeming medical images blurry. For microfluidic applications, dimensions are small so the actual amount of scattering is low. However, to conserve the useful information, removal of the scattered photons is required. Various filtration methods, such as time gating, coherence gating, angular gating, and geometric gating, have been developed in order to selectively reject the scattered photons [18]. This thesis focuses on the use of coherence gating. In order to understand coherence gating, a brief description of coherence length of a light source and interferometry is presented.

“The coherence length of [a] light [source] is defined as the spatial extend along the propagation direction over which the electric field of the light is substantially correlated” (a fixed phase relationship over a certain distance) [19]. For example monochromatic (single wavelength) light sources such as lasers are highly coherent and as a result have a coherence length on the orders of centimeters and meters. In contrast, spectrally broad light sources (for example white light) have a very short coherence length, on the order of micrometers.

The physical principle underlying coherence gating is interferometry, and in particular Low-Coherence Interferometry (LCI) using a spectrally broad light source. LCI

measures the interference between a light beam reflected from a sample and a light beam that has a delay through a reference path. It is only possible for the two beams to coherently interfere when their optical path-length difference is within the coherence length of the spectrally broad light source. Since photons that are scattered lose their phase coherence with the reference beam (due to phase changes upon scattering, traveling a longer path, etc.) they do not contribute to the interference signal, and are effectively filtered out, which is why this technique is referred to as coherence gating [19]. A common example of a coherence gated imaging technique is Spectral Domain Optical Coherence Tomography (SD OCT). SD OCT has proven very useful for biomedical imaging, especially ophthalmology because it can image through turbid media such as tissue and provide high axial resolution of a few microns over a comparatively large depth of field of 1-2 mm [20]. Since SD OCT detects only ballistic (singly back-scattered) photons, the lateral resolution is diffraction limited by the optics.

FCT is a coherence-gated functional extension of SD OCT but is based on fluorescence self-interference further described in the next section. The theoretical concepts of FCT as an interferometric imaging technique are presented in Chapter 2 of this document.

### *1.2.1. Fluorescence Self-Interference*

Unlike light from a laser, which is highly coherent, fluorescent light has low coherence, similar to the sources used in SD OCT. Fluorescent light can interfere with itself when a fluorophore is placed a certain distance away from a reflective surface and is excited. It will emit light isotropically and the reflective surface reflects the backward emitted light to interfere with the forward-directed emission. The key to fluorescence self-interference is that forward and back traveling waves are self-coherent and their interference encodes the distance of the fluorophore from the mirror. This phenomena has been well documented in the literature [21]–[23]. For example, FLuorescence Interference Contrast (FLIC) microscopy measures the change in the total emission intensity (constructive and destructive interference nodes) as a function of the distance from a nearby reflecting surface [24]–[27]. This technique has been used to determine nanometer displacements of a fluorescent molecule above a reflector for applications such as measuring cell adhesion on oxidized silicon. However, the depth

capability of FLIC is limited to a few microns, which is a substantial drawback for biomedical imaging.

Another related technique is Spectral Self-Interference Fluorescence Microscopy (SSFM), which measures nanometer displacements of fluorescent molecules based on spectral phase shift information [28]–[32]. This technique was used to locate fluorescent emitters tagged to the outer membrane of *Shigella flexneri* bacterium [32]. However, phase measurements made directly on an interferometric signal require detection of high contrast fringes, and this technique has low resistance to noise.

The weakness of the methods above is that they are limited to short interaction distances of a few micrometers. In order to get longer depth ranges of hundreds of micrometers, the fluorescence self-interference signal can be resolved spectrally with a spectrometer. By employing a spectrometer, the principles of SD OCT can be applied, and this technique is referred to as fluorescent coherence tomography.

### *1.2.2. Fluorescence Coherence Tomography*

Bilenca et al. used the self-coherence property of fluorescence to demonstrate a coherence-gated functional extension to SD OCT termed Spectral Domain Fluorescence Coherence Tomography (SD FCT) [33]; abbreviated to FCT in this document. FCT is based on spectrally detecting fluorescent self-interference whereby the frequency of the interferometric signal encodes the axial location of the fluorescent emitters. The Fourier detection scheme employed in FCT, described in detail in Chapter 2, improves its robustness to noise compared to SSFM. Using FCT, Bilenca et al. obtained cross-sectional images of fluorescent particles in a scattering medium over hundreds of microns with high axial resolution of a few microns without scanning the beam, sample, or objective lens [33]. By providing both functional and structural information, FCT has extensive potential to become a valuable sensing technique for optofluidic devices.

In a previous publication, we demonstrated the feasibility of combining phase processing with FCT and termed the technique Spectral Domain Fluorescence Coherence Phase Microscopy (SDFCPM) [34]. In SDFCPM the phase information of a fluorescent signal is analyzed in addition to its amplitude, and thereby extracts high

resolution functional imaging in scattering media with molecular specificity. Our preliminary work on SDFCPM was limited to observations of nano-scale oscillations at a single depth location [34].

### *1.2.3. Fluorescence Coherence Tomography for Optofluidic Applications*

In this thesis, FCT is combined with microfluidics to open up new possibilities for biological investigations in optofluidics. This thesis demonstrates the localization of a single flowing fluorescent microsphere in a microfluidic channel, and establishes a technical foundation for the combination of FCT and optofluidics. The localization of a cell in a microfluidic channel has recently been demonstrated to be highly sensitive to the cell's size and stiffness, which in turn is an important biomarker for cell classification [8]. Wu et al. used this concept to differentiate live and fixed (dead) HeLa cells (human cervical epithelioid carcinoma cells) in a mixture. Classification of the living from fixed HeLa cells in the microfluidic channel required a precision of 0.6 μm in the measurement of the location of the cells in the microfluidic channel. In the same report, they also demonstrated the ability to distinguish red blood cells from white blood cells with their optofluidic Lab-on-a-chip device [8]. For this application, a much lower tolerance (5 μm) of the measurement of the cells' position within microfluidic channel was needed because of the comparatively large morphological difference between the cell types.

The concepts developed through this thesis work are important for future development of applications in the miniaturization of molecule specific flow cytometry. Another possible application would be the imaging of stained/labeled microorganisms, such as the nematode *Caenorhabditis elegans* (*C. elegans*) that is used in a variety of biological research areas, to demonstrate high resolution functional imaging in scattering media with molecular specificity [35]. The ultimate goal of these efforts would pave the way for replacing the need for z-stacks in confocal laser scanning microscopy given that FCT acquires axial information simultaneously [36] .

## 1.3. Thesis Organization

This document starts with Chapter 2 presenting the theoretical details of FCT as a low coherence interferometric technique. This is followed by Chapter 3 describing the optical experimental layout and sample characteristics; Chapter 4 describes the fabrication of the optofluidic sample; Chapter 5 presents, analyses, and discusses the optofluidic experimental results; and Chapter 6 concludes the thesis with a description of the system's current limitations and suggests direction for future work.

# Chapter 2. Theoretical Concepts of Fluorescence Coherence Tomography

## 2.1. Introduction

This chapter presents the theoretical concepts of Fluorescence Coherence Tomography (FCT) as a low coherence interferometric technique. It also describes the Fourier analysis of the inteferometric data.

## 2.2. FCT Theoretical Details

Unlike Optical Coherence Tomography (OCT) where an external light source is used, in FCT, fluorescent molecules in the sample are used as the source of light. Since fluorescent light is not coherent, FCT's signal results from fluorescence self-interference and not from a separate strong reference signal as in OCT[33]. The key to FCT is the fluorescence self-coherence which has been well documented in the literature [21]–[26], [28]–[32]. The effect can also be explained "as arising from coupling between the [fluorescent] molecule's radiating dipole and its fictitious mirror image" [23]. It can be further explained quantum electrodynamically in [23]. The fluorescence self-interference effect can also be considered as a wave packet interfering with itself as illustrated by concentric circles in Figure 2-1(a). The solid circles represent the direct emission wave packet of the fluorophore (placed in front of a reference reflector) while the dashed circles represent the fluorescence after reflection from the reference reflector; in the same figure, the optical path length difference between the fluorophore and reference reflector is denoted by $\Delta z$. Hence, FCT is a low coherence interferometric technique where signal is formed based on the amplitudes of the interferometric fringes, generated by a sample and reference reflection.

In the initial work on FCT, Bilenca et al. use two opposing objectives in an interferometer, and combined the light through a beam splitter (BS) to interfere the fluorescence traveling in the forward and backward direction illustrated in Figure 2-1 (b) and zoomed in Figure 2-1 (c). Dichroic mirrors ($DM_1$ and $DM_2$ in (b)) were tuned to transmit the green excitation light (532 nm) to the sample and reflect the emission light (610nm) towards the beam splitter. For clarity the excitation light in (c) is omitted from the $O_2$ path. In this thesis, a common path interferometer was employed; an approach similar to that used by Fromhertz and Goldberg in [24]–[26], [28]–[32], described in detail in Chapter 3 .

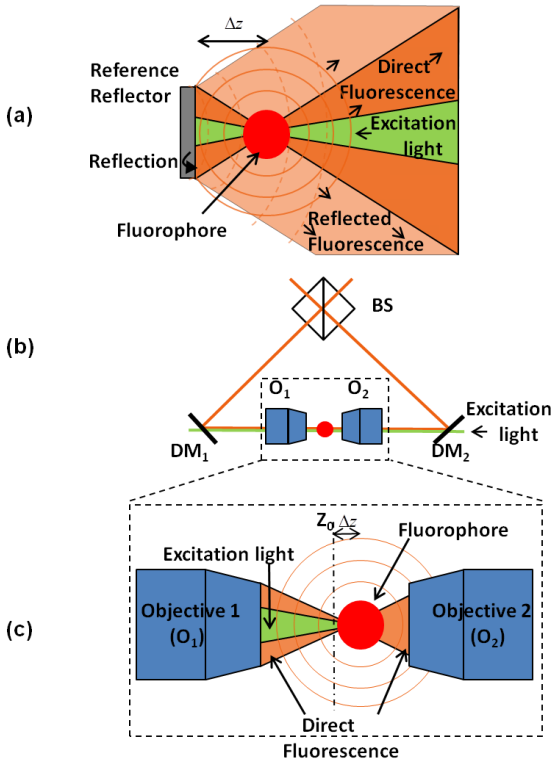


**Figure 2-1: (a) Schematic of the two optical paths of interest for the FCT signal: the direct fluorescence emission path and the fluorescence emission reflected from the reference reflector. Concentric circles represent wave fronts of the emitted light [9]. (b) Initial implementation of FCT by Bilenca et al. use two opposing objectives in an interferometer, light was combined through a beam splitter (BS) to interfere the fluorescence traveling in the forward and backward direction shown in greater detail in (c) with concentric circles representing the wave fronts of the fluorescence [33];**

In Figure 2-1 (a) the reflected fluorescence (with electric field $E_R$) and direct fluorescence (with electric field $E_S$) are shown to originate from a single fluorescent particle. They are combined to interfere and produce fringes as a function of the optical path length difference ($2\Delta z$) given by

$$I(k) = S(k) \cdot \left( {E_R}^2 + {E_S}^2 + 2E_R E_S \cos(2\Delta z n k) \right). \qquad \textbf{Equation 1}$$

where $k$ is the wavenumber of the light, $S(k)$ is the spectral power density, and $n$ is the index of refraction of the medium. The intensity of light, $I(k)$, is given by the magnitude squared of its electric field when light is treated as an electromagnetic wave.

In the case of multiple fluorophores, FCT is a linear system where the interferograms from each fluorescent emitter is linearly combined satisfying the principle of superposition. However due to the self-coherence fluorescence property, the emission from one source is uncorrelated to the other so each emitter will only interfere with itself and not the fluorescence from another source. This is evident through the two cosinusoidal terms in Equation 2 which is an expansion of Equation 1 for two emitters, identified with subscripts 1 and 2, but can be extended for multiple emitters distributed along the same axial dimension.

As in Equation 1, the location of each fluorescent emitter is encoded by the inteferometric frequency modulation of the emission spectrum, given by

$$\begin{aligned} I(k) = S(k\ ) \cdot ( & {E_{R_1}}^2 + {E_{S_1}}^2 + 2E_{R_1} E_{S_1} \cos(2\Delta z_1 n k\ ) + \ldots \\ \ldots + & {E_{R_2}}^2 + {E_{S_2}}^2 + 2E_{R_2} E_{S_2} \cos(2\Delta z_2 n k\ )) \end{aligned} \qquad \textbf{Equation 2}$$

where the frequencies, $\Delta z_1$ and $\Delta z_2$, are proportional to the fluorescent emitters distance from the reference reflector.

To extract the axial location of fluorophores relative to the reference reflector, the Fourier transform of the interferometric signal, $I(k)$ in Equation 1, must be considered resulting in

$$\hat{I}(z) = \hat{S}(z) \otimes \left[ (E_R{}^2 + E_S{}^2) \cdot \delta(z) + 2E_R E_S \cdot \left( \delta(z + \Delta z) + \delta(z - \Delta z) \right) \right] \quad \textbf{Equation 3}$$

where $\hat{S}(z)$ is the Fourier transform of the fluorescence spectrum. The delta functions, $\delta(z \pm \Delta z)$, describe the position of the fluorophore with respect to the reference reflector and $(E_R{}^2 + E_S{}^2) \cdot \delta(z)$ is the non-interferometric components of the signal. The complex conjugate, also known as the mirror affect, arises because the interferometric signal is a real valued function, and as a result the Fourier transformed signal has both negative and positive frequencies (phase is not recorded). In the case where fluorescent emitters are placed above a reflective surface, there is no ambiguity of their position because all FCT particles are to one side of the mirror. For multiple fluorophores ($m = 1,2,3,...,M$) located along the axial dimension of a sample, each fluorophore will generate a delta function, $\delta(z \pm \Delta z_{m=1,2,3,...,M})$, corresponding to their respective locations, $\Delta z_{m=1,2,3,...,M}$.

The coherence length of the fluorescent light, regarded as the source light in FCT, is given by [20]

$$l_c = \frac{2 \ln 2}{\pi} \frac{\lambda_0{}^2}{\Delta \lambda} \quad \textbf{Equation 4}$$

assuming $\hat{S}(z)$ has a Gaussian profile with a full width half maximum (FWHM). $\Delta\lambda$ and $\lambda_0$ are the spectral bandwidth of the fluorescence emission and its central wavelength, respectively. The coherence length dictates the system's axial resolution, which is dependent on the width of the fluorescence spectral range; the wider the spectral range is, the narrower the spread of $\hat{S}(z)$ becomes, increasing the precision of the axial measurement. It also stipulates that fluorophores positioned along the same axial

dimension must be separated by at least the fluorophore's coherence length for them to be resolved. This type of discrete distribution avoids washing out of the fringes.

FCT is based on an optical measurement technique called Low-Coherence Interferometry (LCI). LCI measures interference between light backscattered from a sample and light that has a delay through a reference path. The LCI signal measures the phase differences of the light field [20], [38]. One technique to perform LCI measurements involves scanning the position of the reference path. Using a point detector that incoherently sums the broad optical spectrum generates intensity variations (fringes) as a function of position[20], [38]. The interferometric fringes are only detected when the path length difference ($\Delta z$) of the reference and sample arms are within the coherence length of the system ($l_c$). LCI is the basis of FLIC microscopy [22]–[24].The FLIC signal goes through destructive and constructive interference as a function of distance of the particle from the mirror (it's virtual image), consequently quenching or enhancing the intensity of the emission spectrum. For path length differences between the fluorescent particle and its mirror image that are longer than the coherence length, there is no interference because the electromagnetic fields from the sample and its reflection are uncorrelated

FCT is different from FLIC because it uses a spectrometer detector. In FCT, self-interference can be observed at distances greater than the coherence length ($l_c$) because the detection of the interference is spectrally resolved [20], [38] and can be considered as using a narrow spectral bandwidth filter. Since the coherence length ($l_c$) is proportional to $\lambda_0^{\,2}/\Delta\lambda$ a narrower bandwidth ($\Delta\lambda$) significantly increases the detection coherence length ($l_c$) compared to the total coherence length ($l_c$ ) of the fluorescent emission spectral bandwidth ($\Delta\lambda$). To use representative numbers, a 70nm FWHM spectrum with a central wavelength of 612 nm has a coherence length of 2.3 um, whereas a spectrometer with 0.05nm resolution has a detection coherence length of ~3.3mm. Unlike FLIC where the overall emission intensity is enhanced or quenched due to interference, in FCT, the optical path length differences are encoded by the inteferometric frequency modulation superimposed on the emission spectrum.

In Fourier analysis, the Signal to Noise Ratio (SNR) can be calculated as the signal from the peak value ($\mu$) to the standard deviation of the noise floor ($\sigma$) in decibels (dB) given by [39]

$$SNR_{dB} = 20\log_{10}\left(\frac{\mu}{\sigma}\right). \qquad \textbf{Equation 5}$$

In FCT, the SNR curve increases monotonically with fluorescence power which is beneficial when detecting fluorescent emitters in scattering media [33]. However a high intensity fluorophore also increases the noise floor which could be problematic for detecting weaker fluorescent emitters along the same axial dimension [33] .

## 2.3. Summary

This chapter described the operational principles of Fluorescence Coherence Tomography and the Fourier analysis scheme employed in FCT. The next chapter sets out to describe the sample preparation and FCT system topology used in this thesis.

# Chapter 3. FCT Experimental Methods

## 3.1. Introduction

The ultimate goal of optofluidic FCT is the study of biological samples. This thesis is a poof-of-concept, and uses artificial fluorescent phantom particles to demonstrate the feasibility of combining FCT with microfluidics. This chapter presents the two major components of the FCT system topology: a common-path interferometer and a custom built spectrometer. The phantoms consisted of two types of samples: stationary and optofluidic samples. This chapter describes the preparation of the stationary sample which involved the deposition of fluorescent particles at a fixed distance away from a reference mirror; whereas the optofluidic samples were comprised of flowing particles in a microchannel and is discussed in the next chapter.

## 3.2. FCT System Topology

The FCT system topology is composed of a phase-stable common-path interferometer, and a custom-built spectrometer. In order to assist with sample alignment, a wide field imaging system (microscope) was incorporated with the setup.

The FCT excitation light source used was a frequency doubled Neodymium-doped Yttrium Aluminium Garnet Nd:YAG laser (532 nm) with output up to 6.7 mW. The light source was directed to a 10x objective (Edmund Optics 10X DIN Achromatic Intl Standard Objective, focal length of 16.6 mm, lens diameter of 7.5 mm, working distance 6.3 mm, NA = 0.25), through a 593 nm single edge dichroic beam splitter (Semrock, 593 nm edge Brightline). Instead of scanning the position of the beam, the sample assembly was equipped with linear actuators for x-y-z axis translation.

In the common-path interferometer in Figure 3-1 (a), the objective focused the laser beam down to a waist ($W_0$) of 5.6 μm at the sample with a Rayleigh range ($Z_R$) of 185 μm. The focused waist, $W_0$, is related to the incident beam waist, $W$, on a focusing lens by [40]

$$w_0 = \frac{f\lambda}{\pi w}, \qquad \textbf{Equation 6}$$

while the Rayleigh range is related to $W_0$ by

$$Z_R = \frac{\pi w_0^{\,2}}{\lambda}. \qquad \textbf{Equation 7}$$

Fluorescent light excited at the sample was collected by the same objective, and directed by a dichroic to the detector. Spectrally resolved detection of the fluorescent signal was performed using a custom lens based Czerny-Turner type spectrometer [41], shown in Figure 3-1 (a). The narrow bandwidth of the fluorescent emissions (~70nm FWHM) and use of achromatic lenses alleviated the need for using mirrors (for general and extremely broadband applications). The diameter of the sample light was doubled using a Keplerian beam expander to fully illuminate the diffraction grating (Edmund Optics, 25x25 mm, 1200 lines/mm, blazed) at an incident angle of 75$^o$. In addition, a 593 nm 0$^o$ incident long pass filter (Semrock, 593 nm blocking edge Brightline) was placed right after the beam expander to block any remaining reflected laser light. The first order of diffracted fluorescent light was focused onto the Charge-Couple Device (CCD) detector (Basler Scout scA1390-17gm, 1392 by 1040 pixels, each 4.65 μm square, Ethernet connection to PC) by a 2" achromatic lens with a 100 mm focal length. A custom Labview 8.2 program was used to acquire data.

(a)

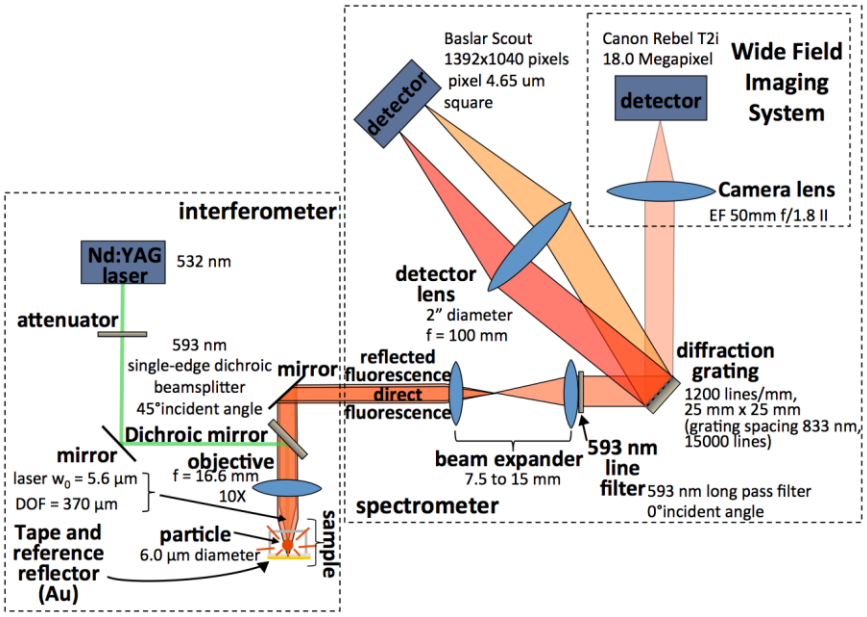


(b)

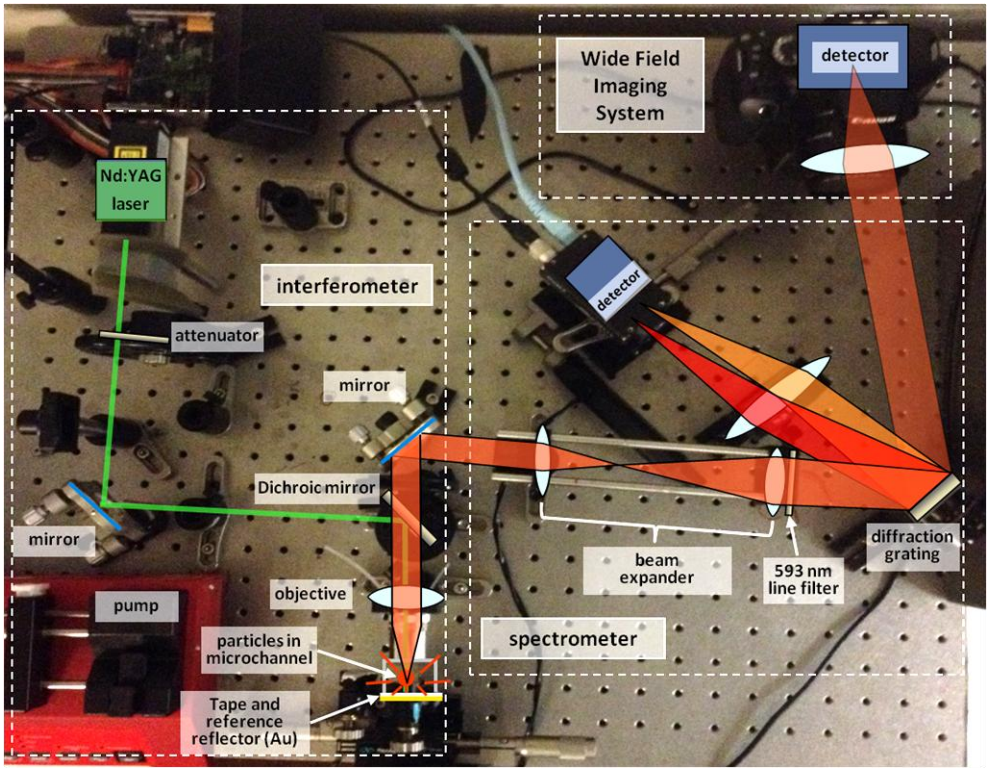


**Figure 3-1: (a) Schematic diagram of FCT setup comprising of a common path interferometer, custom built spectrometer and wide field imaging system. (b) Physical FCT setup in the lab.**

The custom built spectrometer's bandwidth is governed by the grating equation, Equation 8, and is limited by the width of the detector: 6.4 mm. The diffracted light at a diffraction grating is related to the incident light by [42]

$$\frac{m\lambda}{a} = \sin(\theta_i) + \sin(\theta_m), \qquad \textbf{Equation 8}$$

where $m$ is the order of diffraction, $\lambda$ is the wavelength of light, $a$ is the grating spacing ($a$ = 833 nm due to 1200 lines/mm on the diffraction grating), and $\theta_i$ and $\theta_m$ are the incident and diffracted angles respectively. Considering the CCD detector in Figure 3-1 (a), as a one dimensional linear array with a detector lens of focal length, $f$, the linear dispersion is given by

$$y = -fD = -f\frac{\partial\theta_m}{\partial\lambda} = -f\left(\frac{m}{a\cos(\theta_m)}\right), \qquad \textbf{Equation 9}$$

where $D$ is the angular dispersion derived from taking the derivative of Equation 10 with respect to $\lambda$.

The spectral resolution or the minimum resolvable wavelength diffracted off a grating is given by

$$\Delta\lambda_{\min} = \frac{\lambda}{N} \qquad \textbf{Equation 10}$$

where $N$ is the number of illuminated lines on the grating. By using a 25x25 mm diffraction grating with 1200 lines/mm in Figure 3-1 and a center wavelength of 628 nm, $\Delta\lambda_{\min}$ was calculated to be 0.021 nm. Referring back to Equation 9, $\theta_m$ equal to 0°, and with a detector pixel size of 4.65 µm, the spectral bandwidth of one pixel was found to be 0.039 nm/pixel. However, the Nyquist sampling theorem specifies that signals should be sampled at least twice the frequency of the required resolution (to avoid

aliasing) which means that the FCT system is currently limited by the detector resolution and not the grating.

For live wide-field imaging, a non-coherent light source (desk lamp-not show in Figure 3-1) was used to illuminate the sample assembly from the side. As a result, when the lamp was switched on, the microscope objective relayed an image of the sample through the dichroic beam splitter and beam expander to the diffraction grating. Then the sample light was reflected (diffraction order *m* = 0) from the diffraction grating and relayed through a 50 mm focal length lens to the detector (Canon, (EF 50mm f/1.8 II)) as demonstrated in Figure 3-1 (a). The detector was connected via USB to the PC, and controlled through Canon's EOS utility software. This arrangement made it easy to align the laser spot inside the microchannel, observe flowing microspheres, and monitor the generation of fluorescence interference patterns simultaneously in the Labview program. For further demonstration and understanding, the system's schematic and actual implementation of the system is shown in Figure 3-1(a) and (b), respectively.

## 3.3. Data Processing

As detailed in Chapter 2, the Fourier analysis of the spectral interferometric signal, $I(k)$, extracts the location of the fluorophores above a reflective surface. However before performing the Fourier transform of the interferometric signal, $I(k)$ in Equation 1, a few data processing steps are required such as: DC subtraction, linear sampling, Hann windowing, and sample padding. DC subtraction refers to removing the non-interferometric components of the signal in Equation 1, $E_R{}^2$ and $E_S{}^2$, that have a specific profile that is related to the fluorophore's emission spectrum in Figure 3-2. Referring back to Equation 1, the terms, $E_R{}^2$ and $E_S{}^2$, are removed by curve fitting $I(k)$ with a polynomial of degree 4 in a least squares sense and subtracting it from $I(k)$. The remaining term $2E_R E_S \cos(2\Delta znk)$ represents the interferometric signal to be processed. Next, the frequency of the cosine term in Equation 1 is a function of wavenumber, $k$, but the interferometric signal is (approximately) linearly distributed in

wavelength, $\lambda$ , across the spectrometer. In addition, $k$ is inversely proportional to $\lambda$ given by

$$k = \frac{2\pi}{\lambda}, \qquad \textbf{Equation 11}$$

so the signal has to be resampled to be linear in $k$ ,spaced in increments of $\delta_k$ defined as:

$$\delta k = -\frac{2\pi}{\lambda^2}\delta\lambda. \qquad \textbf{Equation 12}$$

To further improve the results of the Fourier transform, the resampled interferogram is multiplied by a Hann window and is zero-padded to decrease the presence of side lobes and increase the number of interpolated points in the Fourier transformed space, respectively. After performing these processing steps, the $z$ values can be computed by the Fourier transform of the interferometric data with a distance range from $-z_{max}$ to $+z_{max}$ (in µm) given by

$$z_{max} = \frac{\pi}{2n\delta_k}, \qquad \textbf{Equation 13}$$

in increments of $\delta_z$ given by

$$\delta_z = \frac{2 \cdot z_{max}}{n-1}. \qquad \textbf{Equation 14}$$

The detection bandwidth of the spectrometer was calculated to be 70 nm ranging from 593 to 663 nm, providing a $\delta\lambda$ of 0.05 nm/pixel. Referring to Equation 12 and with $\lambda$ = 628 nm, $\delta k$ was calculated to be 796 $m^{-1}$. This allowed for a maximum displacement , $z_{max}$ , of approximately 2 mm determined by Equation 13. In addition, referring to

Equation 4, the coherence length was calculated to be approximately 2.3 μm (assuming a ~70nm FWHM).

## 3.4. Fluorescent Sample Preparation

Fluorescent beads were used as the light sources of the FCT signal. Previously, investigating phase sensitive measurements of the FCT signal, fluorescent microspheres with a mean diameter of 0.11 μm were used [34]. In order to model cells in a microchannel a larger sized phantom was required. Therefore, 6 μm in diameter polystyrene microspheres (36-2FMT, Thermo Scientific, MA) were chosen to match the average diameter of human red blood cells (nominally 7-8 μm in diameter [43]). The 6 μm microspheres are dyed throughout with a proprietary "Firefli$^{TM}$" dye manufactured by Thermo Scientific. The "Firefli$^{TM}$" excitation and emission spectra have peaks at 542 nm and 612 nm, respectively, corresponding to a Stoke's shift of 70 nm. This is demonstrated in Figure 3-2 [44]. With a wide excitation band between 525 and 550 nm and peaking at 542nm, using a frequency-doubled ND: YAG laser at 532 nm as the excitation source was well matched.

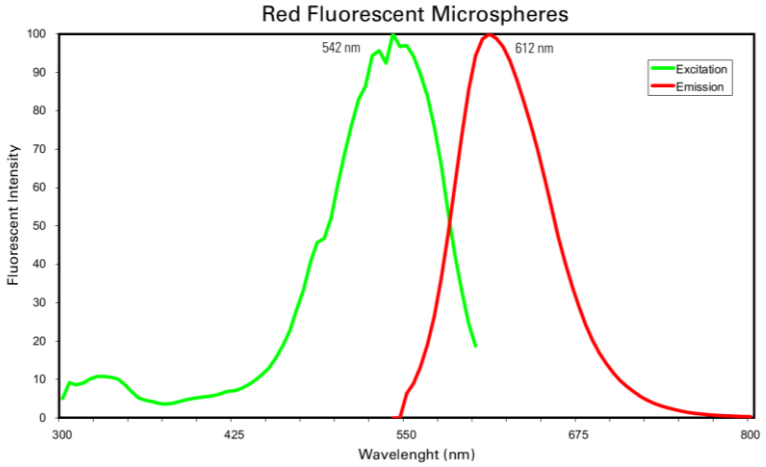


**Figure 3-2: Excitation (green) and emission (red) spectra of the 6 μm microspheres dyed with proprietary "Firefli$^{TM}$" dye** [44]**.**

To use the microspheres, it was necessary to immerse them in an aqueous solution and serially dilute them to obtain a low enough concentration. This guaranteed that the detection of fluorescent emission was due to single particles in both stationary and optofluidic sample configurations.

A set of different concentrated solutions of microspheres (1, 0.14, $2x10^{-3}$, $4x10^{-6}$, $8x10^{-9}$ mg/ml) were prepared in an ethanol water mixture and deposited on a microscope slide. They were left to dry in room temperature for observation under a microscope. Visual inspection determined that the 0.14 mg/ml mixture contained sparse single particles and this was further verified through flow experiments, explained in Chapter 5.

### *3.4.1. Stationary Samples*

To demonstrate the acquisition of FCT data, stationary samples were required. . Hence a convenient and simple sample was devised: a serially diluted deposition of 6 µm microspheres on a single strip of double sided tape (Scotch® Permanent Double Sided Tape) adhered to a gold coated microscope slide (EMF Corporation, CA136 (Cr/Au)). The basic configuration of this sample is illustrated in Figure 3-3. By using gold as the reflective surface in the configuration below, it was possible to record interference patterns from single microspheres due to its high reflectivity of $R$~ 0.9 in the visible range [45] .

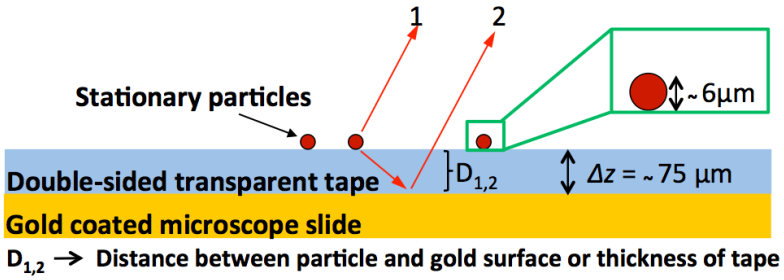


**Figure 3-3: Schematic diagram of the stationary samples consisting of fluorescent microspheres deposited on double sided transparent tape adhered to a gold coated microscope slide. Fluorescence emission is divided into two components: rays 1 and 2 and their interference decode the distances: $D_{1,2}$.**

To calculate the optical distance, $\Delta z$ from Chapter 2, the index of refraction, $n$, of double sided tape is required (Equation 1). Although the manufacturer does not provide this product detail, the experimental analysis reported in Chapter 5 used $n$ = 1.4740 ± 0.0005 (at 589.3 nm at 25 $^{o}$C). This detail is specified by Thorlabs Inc., a distributor of 3M's optically clear double sided- tape [46] .

## 3.5. FCT Thickness Measurements of Double Sided Tape

After the stationary sample was prepared, it was placed in the interferometer configuration shown in Figure 3-1. There are two optical paths of interest for the FCT signal: the direct fluorescence emission (in the direction of the objective) and the fluorescence emission reflected from the gold coated microscope slide shown as rays 1 and 2 in Figure 3-3, respectively. For the remainder of this document, the gold coated microscope slide is also referred to as the mirror. The spatial separation between the fluorophore and mirror introduces phase differences between these two components. These components then interfere with each other and result in an interference pattern (fringes) given by Equation 1 in Chapter 2.

With the laser power at 0.8 mW and the CCD programmed with 0 dB analogue gain and an integration time of 55 ms, the interferometric fringes acquired by the spectrometer is shown in Figure 3-4 (a).This interference pattern (fringe frequency) corresponded to the distance of the fluorophore from the mirror, $D_{1,2}$ , which is in fact the thickness of the double sided tape, $\Delta z$, in Figure 3-3.

By vertically binning the 41 rows of data in Figure 3-4 (a) it was possible to obtain an intensity profile of fringes as a function of wave number, shown in Figure 3-4 (b). By subtracting the DC from the signal in Figure 3-4 (b), a more uniform intensity profile was acquired, shown in Figure 3-4 (c) which as stipulated in section 3.3 is required before performing the Fourier transform. The uneven intensity was due to two reasons: first, the spectral shape of the "Firefli" dye's fluorescent emission has a bell shape as in shown in Figure 3-2. Secondly, the dichroic mirror and long pass filter used in the optical setup in Figure 3-1 were designed to transmit light past 593 nm, effectively cutting off almost all the left portion of the fluorescent emission spectrum shown in Figure 3-2.

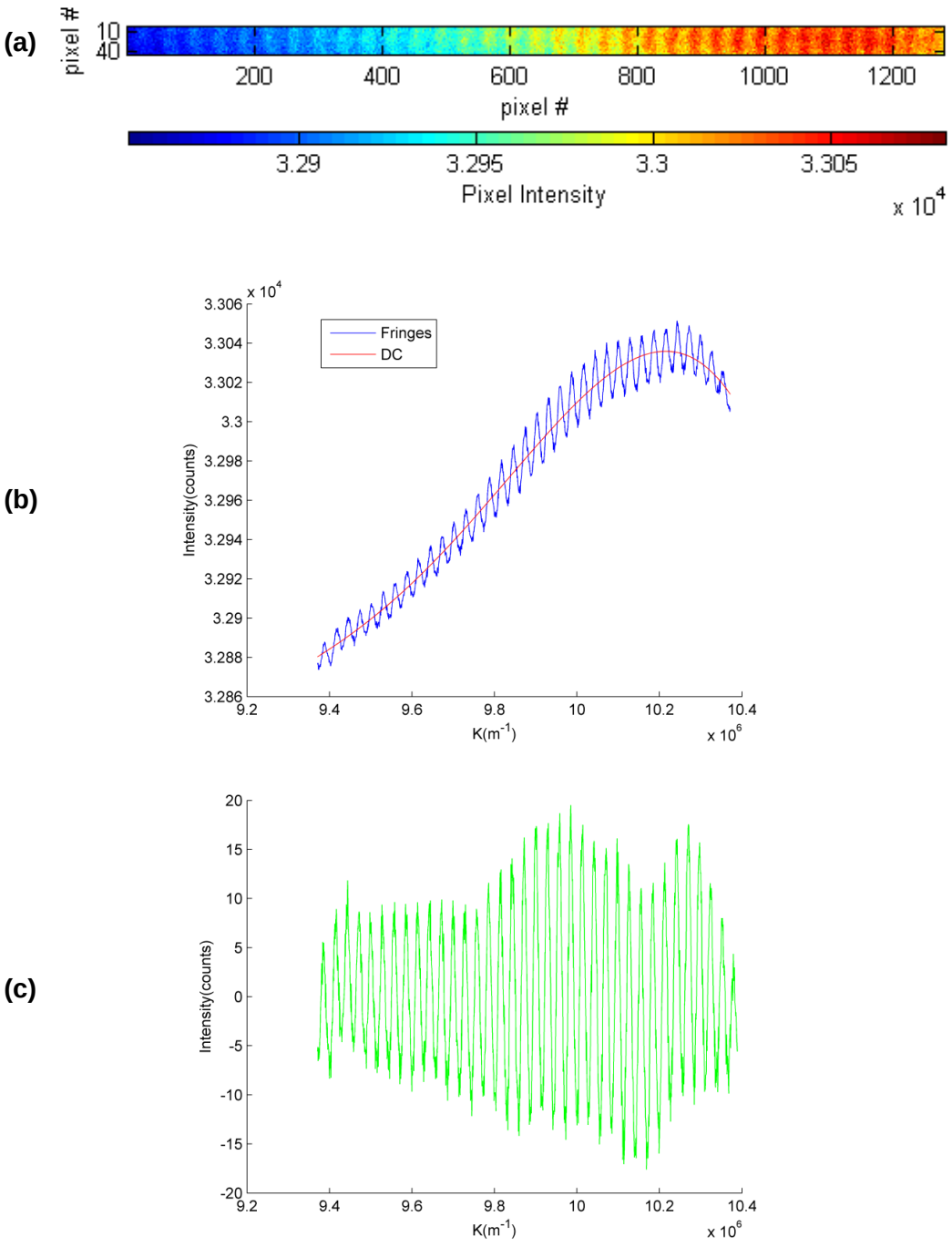


**Figure 3-4: (a) Interferometric data acquired from fluorescent microspheres deposited on double sided tape. False color heat map used to display intensity. (b) Intensity profiles of fringes for double sided tape thickness. (c) Intensity profiles of fringes after subtraction of linear component.**

To confirm that the interferometric measurement of the path length, $\Delta z$, was consistent with the thickness values provided by the manufacturer and distributor of Scotch® Permanent Double Sided Tape[47][46] the Fourier transform of the intensity profile in Figure 3-4 (c) was taken. The resulting frequency transform was normalized and plotted as a function of $z$ shown in Figure 3-5. The peak identified by blue markers can be reasonably approximated as a Gaussian with FWHM of ~4.5 μm and its location corresponded to the thickness of the double sided tape. A "non-linear least squares" Gaussian fitting method of the data points indicated by blue markers in Figure 3-5 obtained a path length, $\Delta z$, of 75.0 ± 2.3 μm (the center of the peak ± the coherence length). This was in agreement with the manufacturer's specification of the tape thickness value of 76.2 um with a surface roughness of 2.6 um [47] and with the specification value of 75 um provided by a distributor, Thorlabs Inc [46]. The SNR of the peak in the Fourier domain (expressed as the ratio of the peak height (μ) to the surrounding noise (σ)) defined in Equation 5 in Chapter 2 was calculated to be 35.17 dB.

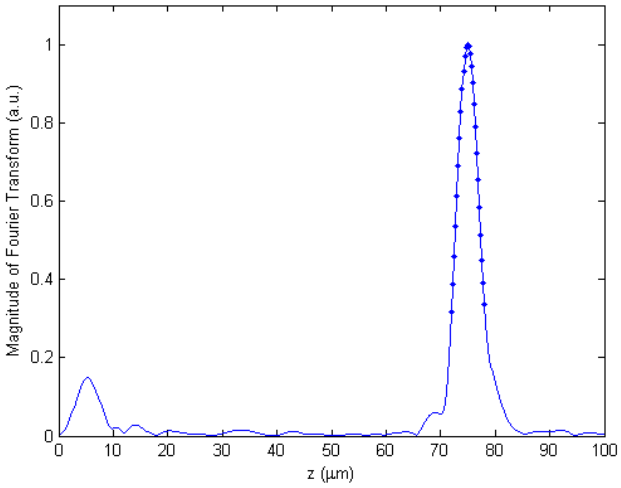


**Figure 3-5: Fourier transform of the fringe profile in Figure 3-4 (b) with blue markers indicating the region of the curve used for calculating $\Delta z$. The peaks have been normalized.**

This experimental thickness finding was consistent with other thickness measurements taken with different pieces of tape from the same roll. In spite of this, to improve the accuracy of this finding, it would be necessary to perform multiple measurements with tape sheets from different rolls of the same type of double sided

tape. However, the tape was used first and foremost as an adhesive layer between the microchannel and gold coated microscope slide. In addition since it was possible to measure fringes with a reasonable SNR the aforementioned configuration sufficed.

## 3.6. Summary

This chapter introduced the FCT system topology with its optical parameters and fluorescent particle characteristics. This was followed by a description of the stationary sample configuration in which fluorescent microspheres were deposited on a double sided tape adhered to a gold-coated microscope slide. It concluded with FCT thickness measurements of the double sided tape used in the stationary sample which matched the manufacturer's thickness specifications. The next chapter discusses the fabrication of an optofluidic sample for optofluidic experiments.

# Chapter 4. Optofluidic Sample

## 4.1. Introduction

This chapter introduces the microfabrication of the optofluidic sample consisting of flowing fluorescent microspheres through a straight microfluidic channel. The material used for the microfluidic channel was polydimethylsiloxane (PDMS). PDMS is an optically transparent elastomer making it a suitable material for fabrication of devices that are optically interrogated [15]. In addition, PDMS offers simple processing techniques and is biocompatible due to its non-toxic nature [15]. The following sections describe the fabrication and characterization of the master mold used to produce microchannels, the fabrication of the optofluidic sample using the master mold, and the methods used to conduct flow experiments.

## 4.2. Master Mold Design and Fabrication

Common materials used in microfluidics are silicon, glass, and polymers. These materials can be patterned using photolithography, similar to that used in integrated circuit fabrication. The first step for fabricating the microfluidic channels used in this thesis was to create a master mold from which polymer replicas can be generated. This procedure allows for rapid and inexpensive prototyping. The master mold was made using standard photolithography techniques of patterning permanent epoxy negative photoresist SU-8 (2025 MicroChem, MA). The process involved spinning of SU-8 onto a silicon wafer, soft baking, defining the SU-8 structures by exposure to UV light using the mask in Figure 4-1, post-exposure baking, and lastly SU-8 development. This process flow is further described in details in Figure 4-3. The microfluidic channel measured 3 cm in length with a rectangular cross section of 218 μm in width and 28 μm in height. The target height of the channel was 50 μm however 28 μm was the tallest height achievable within the processing of the lab. The square reservoirs were 5 by 5 mm.

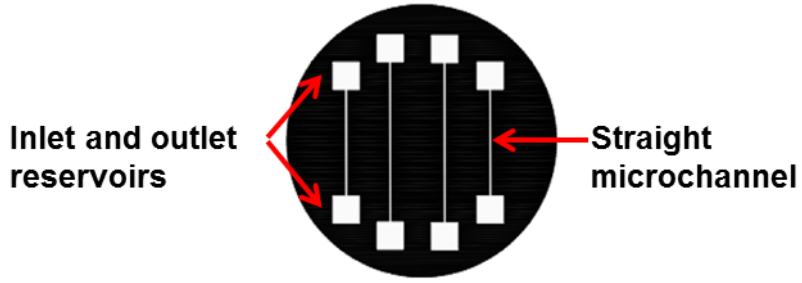


**Figure 4-1: Photomask used to fabricate the master mold.**

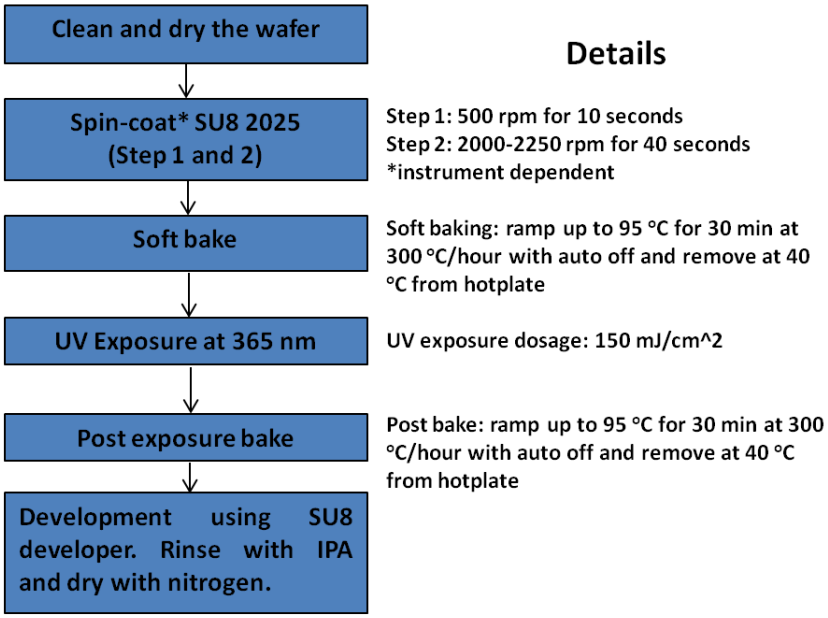


**Figure 4-2: Process flow with parameter details for fabricating master mold.**

### *4.2.1. Microfluidic Channel Characterization*

The Profilometer (KLA Tencor Alpha-Step 500) traces shown in Figure 4-3 measured the height of the SU-8 channels in the master mold to be 28.64 µm in height and 218.4 µm in width. The data in Figure 4-3 (a) shows a bulge on the left side of the trace encircled in red which is due to the delayed response of the profilometer needle head in detecting the height change as it encountered the channel wall and therefore, continued dragging the wafer across the sample platform for approximately 110 µm. In spite of this problem, the height measurement was not affected. However, regardless of

the previous measurement, a new trace was performed to measure channel width shown in Figure 4-3 (b). In this characterization setup only one measurement at a single position across the microchannel was recorded. In future work, enhanced accuracy can be attained by recording trace measurements at different positions along the 3 cm long channel to account for any variations in the thickness of the SU-8 layer.

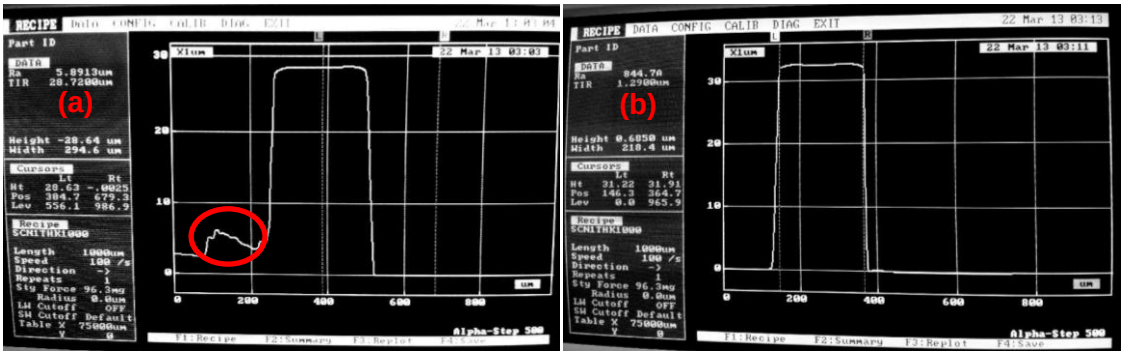


**Figure 4-3: A profilometer trace conducted on the SU-8 master mold using a KLA Tencor Alpha-Step 500. (a) Microchannel height measurement. (b) Microchannel width measurement. The traces are represented with an aspect ratio (width: height) of 20:1. The red circle indicates the delayed response of the profilometer needle head in detecting the height change as it encountered the channel wall.**

### *4.2.2. Microfluidic Channel Fabrication*

The microfluidic device was fabricated with PDMS (Sylgard 184, Dow Corning, MI) using the standard soft lithography technique[48]. For FCT, the thickness of the PDMS layer at the channels is critical and is required to be less than the working distance of the objective (6.3 mm in air). The thickness of the PDMS layer at the channel was maintained at ~3.7 mm. PDMS is prepared by mixing the elastomer base with crosslinker at a 10:1 weight ratio using a stirring spoon, and then the solution is degassed under vacuum for about one hour. After degassing, the mixture is poured onto the patterned SU-8 master and left to cure overnight at room temperature. The next day, the PDMS film was separated from the mold master. Holes were punched into the reservoirs for inlet and outlet ports for inserting polyethylene tubing (Intramedic, PE 190 ID 1.19 mm). The PDMS was tape bonded (Scotch® Permanent Double Sided Tape) to a gold coated microscope slide, and baked for 2 hours at 80 $^{o}$C following the processing steps in Figure 4-4 (a-c) [49]. This fabrication technique allowed the production of device

replicates shown in Figure 4-4 (d). As in Chapter 2, the gold coated microscope slide acted as the reference reflector for the fluorescent emission from fluorescent particles within the channel.

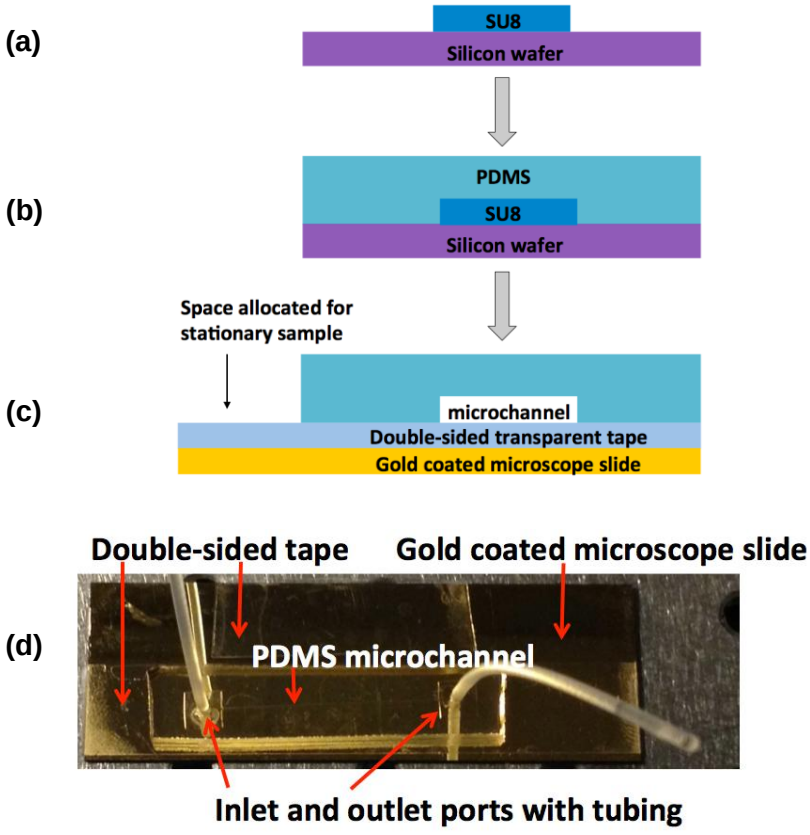


**Figure 4-4: Fabrication process for bonding PDMS to gold coated microscope slide. (a) SU-8 is fabricated on a silicon wafer using photolithography. (b) PDMS is poured on the master and left to cure overnight. (c) The PDMS replicate is detached, punched with inlet holes, and is placed onto one side of the double sided tape. The other side is adhered to a gold coated microscope slide. The device is baked at for 2 hours at 80 °C to finalize bonding. (d) Physical microfluidic device.**

### *4.2.3. Flow Method*

After the optofluidic sample was prepared, it was placed in the interferometer configuration shown in Figure 3-1. The excitation laser was focused to a spot size, $w_{0,}$ of 5.6 μm. The CCD detector in the spectrometer was set with an exposure of 55 ms. In

order to get a sufficiently strong fluorescence interference signal, the ideal case would be to have a fluorescent particle in the focal volume for the duration of an integration period of the CCD detector, illustrated in Figure 4-5 (a). Assuming the width of that volume to be 10 µm ($2*w_0$), the height and depth of the channel to be 220 and 28 µm respectively, and exposure set at 55 ms, the maximum flow rate was calculated to be 0.0672 µl/min. This was below the slowest flow rate of 0.08 µl/min specified by the syringe pump available (NE-300 Just Infusion™ Pump) with a 1 ml syringe. To overcome this limitation during the experiment, the channel was vertically orientated as illustrated in Figure 4-6 leaving gravity as the force to actuate the microfluidic flow. The syringe pump was used to inject particles to the inlet port with a flow rate of 30 µl/min. After detecting flowing microspheres in the channel with the wide field imaging system(shown in Appendix A), the pump was switched off. This led to a flow rate that was slow enough for detecting the generated fluorescence interference, explained in the next chapter.

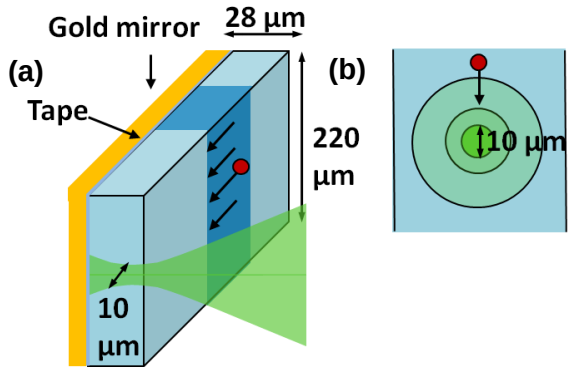


**Figure 4-5: Flow calculation. (a) Oblique side view, (b) front view of particle flowing through the laser interrogation site. The green concentric circles indicate the Gaussian laser beam with intensity highest in the center at $w_0$**

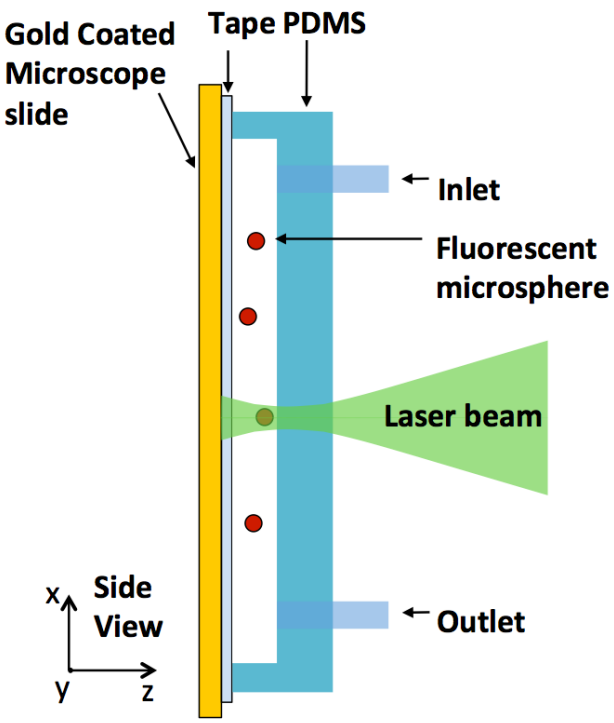


**Figure 4-6: Side view illustration of experimental method for dynamic samples.**

## 4.3. Summary

Polymer microfabrication follows relatively straight forward processing steps. The fabrication of the final device was simplified by using double sided tape to bond the polymer to the gold coated microscope slide. PDMS does adhere to silicon, but it does not have high reflectivity in the visible range. Gold does not adhere strongly to PDMS and in preliminary efforts a strong bond was not made. The double sided tape fulfilled an additional role: it acted as an offset of known thickness separating the fluorophore from the gold surface, setting a minimum distance for the interferometric measurements.

This chapter presented the fabrication steps for a microfluidic channel. In the context of the optofluidic device, this channel will be used for flowing microspheres through the FCT acquisition system. The next chapter describes the experimental results of using FCT on optofluidic samples.

# Chapter 5. Optofluidic Experimental Results

## 5.1. Introduction

This chapter presents the FCT interferometric measurements for the optofluidic sample that was described in Chapter 4, consisting of flowing fluorescent microspheres through a straight microfluidic channel. Two experimental configurations are presented. The first experiment was conducted with a single laser source for proof of concept. The second experiment used two laser sources to demonstrate the ability for parallelism in the measurement technique and demonstrate proof of concept for line-field imaging capabilities.

## 5.2. Experimental Method

To perform FCT acquisition on the flowing microspheres, the optofluidic sample in Figure 4-4 (d) was placed in the interferometric configuration shown in Figure 5-1(a) and was connected to the syringe pump via the tubing. As the laser interrogated the flowing microspheres in the microfluidic channel, the fluorescence emission was divided into three components, one that was directly collected into the CCD detector, one that reflected off the mirror (gold coated microscope slide), and one that reflected off the surface of the double sided tape prior to being collected; illustrated as rays “1”, “2”, and “3” respectively in Figure 5-1 (b). The optical path-length differences between the three components labeled in Figure 5-1 (b) represent: $D_{1,2}$, the distance between microsphere and the mirror; $D_{3,2}$, thickness of double sided tape; and $D_{1,3}$, the distance between the particle and tape. These terms generated the interferometric fringes at the CCD detector which was either displayed in unprocessed form, or analyzed and displayed in real time with the Labview program presented in Appendix A. During acquisition, the raw data was saved to disk for post-processing and detailed analysis of the distances between the flowing microspheres and the mirror.

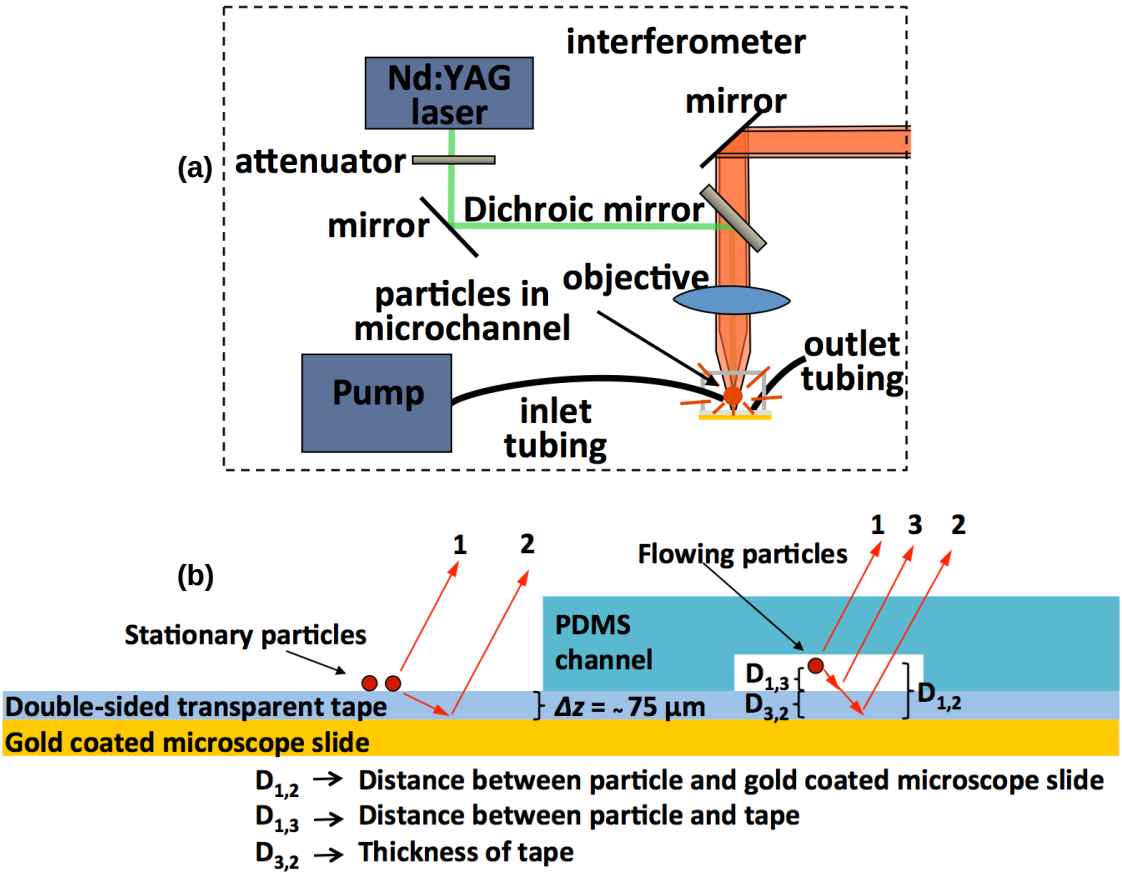


**Figure 5-1 : (a) The optofluidic sample in Figure 4-4 (d) was placed in the interferometer configuration and was connected to the syringe pump via the tubing. (b) Fluorescence emission in the microfluidic channel is divided into three components, one that is directly collected into the CCD detector, one that reflects off the mirror (gold coated microscope slide), and one that first reflects off the surface of the double sided tape prior to being collected, illustrated as rays "1", "2", and "3" and their interference encodes the distances: $D_{1,2}$, $D_{1,3}$, $D_{3,2}$.**

## 5.3. Experimental Results Using One Laser Source

In the first experiment to demonstrate FCT and optofluidics, a single laser source was used. Following the optical design presented in Chapter 3, the spot size was 5.6 µm in the microfluidic channel. The laser power was set at 2.5 mW (after the objective). In order to detect faint fluorescence without introducing significant noise, the CCD detector was set with an analogue gain of 0 dB and an integration time of 55 ms. The data processing was performed following the same steps as outlined in section 3.5. Figure 5-2 shows the results of the data processing steps for a single frame of the fluorescence signal from a flowing particle: (a) 33 rows of interferometric data (for this case), (b) vertically binned intensity profile of the rows from (a) shown in blue with a superimposed interpolated DC shown in red, and (c) intensity profiles of fringes after DC subtraction. Next, the Fourier transform of the interferometric fringe signal was computed as illustrated in Figure 5-2 (d). In Figure 5-2 (d), two peaks are visible, the first peak identified with blue markers corresponded to $D_{3,2}$, the thickness of double sided tape. The second peak identified with red markers corresponded to $D_{1,2}$, the distance between the microsphere and the mirror. $D_{3,2}$ and $D_{1,2}$ were measured as 76.9 ± 2.3 µm and 100.2 ± 2.3 µm, respectively, given by the center of the peak ± the coherence length. By subtracting $D_{3,2}$ from $D_{1,2,}$ the position of the fluorescent particle in the channel away from the tape, $D_{1,3}$, was calculated to be 23.3 µm ± 4.6 µm. The error was propagated by adding the absolute value of the errors.

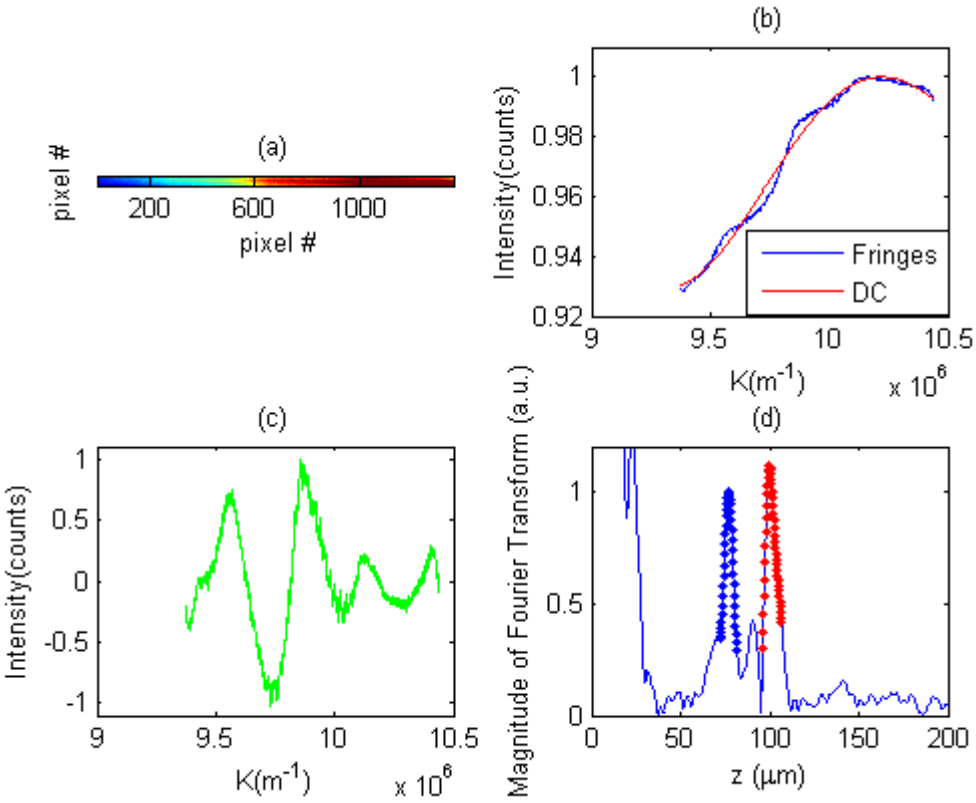


**Figure 5-2: (a) Interferometric data acquired from fluorescent microspheres in microchannel. (b) Intensity profile of fringes (vertically binning of the 41 rows of data in (a)) with superimposed interpolated DC component in red. (c) Intensity profile of fringes after DC subtraction. (d) Fourier transform of the fringe profile in (c) with blue markers indicating the region of the curve used for calculating Δz and red markers indicating the region of the curve used for calculating particle position from the mirror. The peaks have been normalized.**

Next, acquisition was demonstrated for multiple particles. The FCT acquisition of particles flowing through the microchannel was collected for another 5.5 seconds (100 frames with 55 ms of exposure each). All of the frames with particles interrogated by the laser were processed as described above, and the Fourier transformed results (e.g. Figure 5-2 (d)) were concatenated and are shown in Figure 5-3. The horizontal red line in Figure 5-3 presents the approximate thickness of the tape, $D_{3,2}$ , measured as approximately 75 µm, and the red circles indicate the position of the fluorescent particle away from the mirror, $D_{1,2}$ . The position of the fluorophore in the microfluidic channel was calculated by subtracting the tape thickness, ~75 µm, from the position of the

particle away from the mirror. The SNR for each measurement was calculated with the peak values, μ, from the $D_{3,2}$ peaks. The SNR values, the measured positions of the particles away from the mirror, and the measured positions of the particles away from the tape from six events labelled 1 to 6 in Figure 5-3 are presented in Table 5-1. In Figure 5-3, the *z*-axis (vertical axis) starts at 20 μm due to the strong intensity low frequency noise in the 0 to 20 μm range. The use of the doubled sided tape helped to circumvent this low frequency noise problem by acting as an offset of known thickness separating the fluorophore from the mirror, setting a minimum distance of ~75 μm for the interferometric measurements.

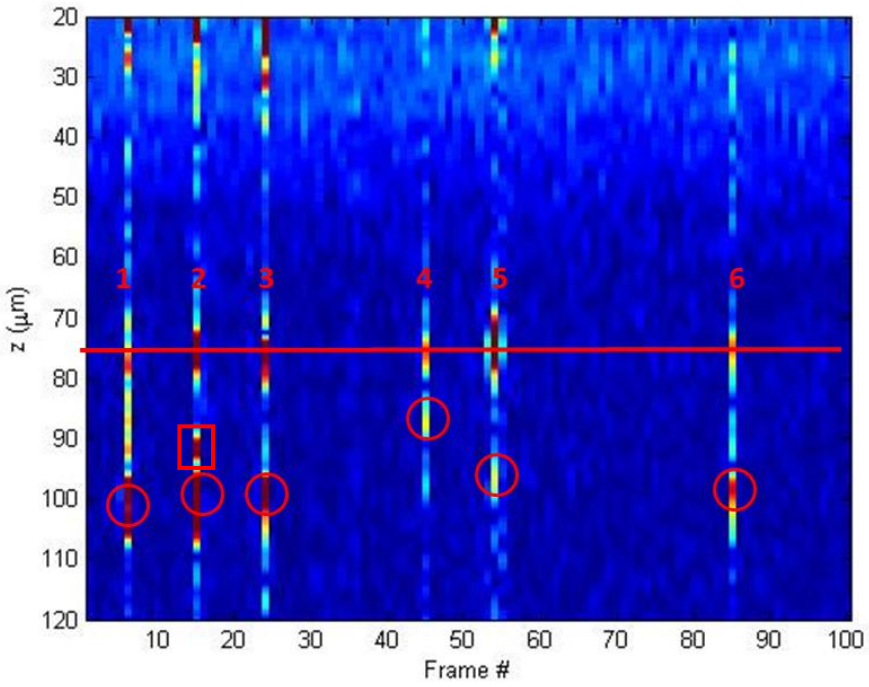


**Figure 5-3: Six consecutive events, labelled 1 to 6, representing interrogated flowing fluorescent particles. The red line indicates the location of the tape. The location of particles (with respect to the mirror) are circled in red. The red square indicates a second particle in event 2. For display purposes, the contrast of the image (dynamic range was reduced) has been enhanced and the z-axis (vertical axis) starts from 20 μm due to the presence of low frequency noise in the 0 to 20 μm range.**

**Table 5-1: SNR analysis of the first peaks in Figure 5-3 with corresponding peak locations, $\Delta z$. $D_{3,2}$ is the thickness of double sided tape while the second peak identified with red circles corresponded to $D_{1,2}$, the distance between microsphere and the mirror. The variation (±) for columns 1 and 2 are calculated by taking the standard deviation of their respective row entries with arbitrary units (a.u). Errors were calculated using the standard error propagation rules.**

| **Particle #** | **μ** ± 161.2 a.u | **σ** ± 13.3 a.u | **SNR** (μ/σ) a.u | **$SNR_{dB}$** (20*log(μ/σ)) dB | **$D_{3,2}$** ± 2.3 μm | **$D_{1,2}$** ± 2.3 μm | ***Particle's position away from tape*** ($D_{1,2}$ -$D_{3,2}$) ± 4.6 μm |
|---|---|---|---|---|---|---|---|
| 1 | 532.0 | 53.4 | 9.9 ± 4.1 | 19.9 ± 3.5 | 75.1 | 98.6 | 23.5 |
| 2 | 771.6 | 49.5 | 15.5 ± 5.8 | 23.8 ± 3.2 | 75.3 | 98.9 | 23.6 |
| 3 | 566.1 | 26.1 | 21.6 ± 13.9 | 26.6 ± 5.6 | 77.2 | 98.8 | 21.6 |
| 4 | 340.6 | 20.1 | 16.9 ± 15.0 | 24.5 ± 7.7 | 75.7 | 87.3 | 11.6 |
| 5 | 643.8 | 21.4 | 30.0 ± 22.5 | 29.5 ± 6.5 | 74.6 | 96.6 | 22.0 |
| 6 | 382.1 | 22.9 | 16.6 ± 13.0 | 24.4 ± 6.8 | 75.3 | 98.8 | 23.5 |

Since the depth of the channel is 28 μm, a maximum of 3 fluorophores located along the same axial line and separated out by the fluorophore's coherence length can be resolved. Two particles were detected in Figure 5-3 in event 2. The first particle was located at 91.6 ± 2.3 μm while the second particle at 98.9 ± 2.3 μm reported in the second row of Table 5-1.

This experiment was a proof of concept demonstrating the integration of FCT with microfluidics (and optofluidics), suggesting that FCT would be able to do this for fluorescently labeled cells as well. To extend this experiment to biological specimens, for example using tagged living cells in place of fluorescent particles, the laser power levels would have to be addressed to avoid photo damage to the cells. With a 532 nm laser, a laser intensity greater than 3.5kW/cm$^2$ (or a power greater than 1.17 mW for the spot size used), has been shown to have photo damage in *Escherichia coli* (*E.coli)* cells [50]. In this experiment, the laser power was set at 2.5 mW, equating to light intensity of 6.4kW/cm$^2$ at the sample. However, it is important that the fluorescent signal obtained, when using power levels that are appropriate for living cells, still maintains sufficient SNR. On the other hand, laser power levels can be optimized to maintain sufficient SNR if the cells are not required for other experiments after laser interrogation. Another important factor governing SNR in FCT is the detector's exposure time. As described in section 4.2.3, the exposure is interrelated with the flow rate. In order to get a sufficiently strong fluorescence interference signal, the ideal case would be to have a fluorescent particle in the focal volume for the duration of an integration period of the CCD detector. By increasing the laser power and accepting the potential photo damage to cells, the exposure duration can be reduced and flow rate increased. The benefit of increasing the flow rate would be higher a throughput of particles. Another way to increase SNR would be to increase the gain of the detector however increasing the gain on the available detector introduced significant noise preventing the detection of faint fluorescence. This could be resolved by purchasing a more sensitive detector such as Electron Multiplying CCD.

Additional validation experiments would have to be conducted before undertaking a biological investigation. For example, to demonstrate measurement of positional variation due to morphological parameters, an experiment with two different sized microspheres would need to be performed. This would represent the case of different cell types, such as identifying red blood cells from white blood cells. For the case where the morphological differences are smaller, such as identifying live versus fixed HeLa cells [8], additional processing steps, such as phase processing [34], would need to be investigated to extract positional differences of the particles that are less than the coherence length of the fluorescent emission.

In this experiment, the laser was focused at the center of the channel therefore limiting the optical detection system to fluorescent particles flowing right at the center and missing out on particles flowing off center. To overcome this limitation, a cross-sectional image of fluorescent particles flowing through the channel could be obtained by either scanning the microfluidic channel or laser perpendicular to the direction of flow. Alternatively, a laser line focus with a non-confocal imaging spectrometer configuration can be used to obtain the cross-sectional image [33].

## 5.4. Experimental Results Using Two Laser Sources

Line field imaging would allow the user to interrogate particles whose path is not centered in the microfluidic channel and particles flowing side by side. By implementing a line scan excitation scheme with a width equal to the cross sectional width of the microfluidic channel (of ~220 µm), all particles flowing through would be interrogated. Implementation of a line field illumination is beyond the scope of this thesis, but it is discussed in more detail in the future work section in Chapter 6.

To demonstrate that the optical system could in fact be capable of line-field imaging, two lasers were used to generate fluorescence interference from two fluorescent particles simultaneously. The second laser was introduced to the interferometer with a beam splitter and an additional turning mirror, illustrated in Figure 5-2 (a). The first laser was set with a power of 2.5 mW while the second laser with a power of 3.2 mW. Due to the unavailability of appropriate neutral density filters, it was not possible to equalize the powers between both lasers. The two laser spots were aligned vertically along the length of the microfluidic channel in Figure 5-4 (b) with a separation of 220 µm from their centers. This was done to demonstrate concepts of parallelism in the measurement technique without changing the overall configuration of the optical system. Figure 5-4 (c) demonstrates simultaneous detection of fluorescence interference from two interrogated particles labeled “1” and “2” corresponding to the laser spots “1” and “2” in (b), respectively. Figure 5-4 (d-e) are the Fourier transformed interferometric fringes from spectra 1 and 2 in Figure 5-4 (c). Figure 5-4 (d) reveals only one peak fitted with blue markers indicating that the fluorescent particle was flowing on the surface of the tape. The peak was measured to be at 74.8 ± 2.3 µm. In Figure 5-4

(e), the second particle was located at 94.2 ± 2.3 µm away from the mirror with a tape thickness of 73.1 ± 2.3 µm. This meant that the particle was located at 21.1 ± 4.6 µm away from the tape.

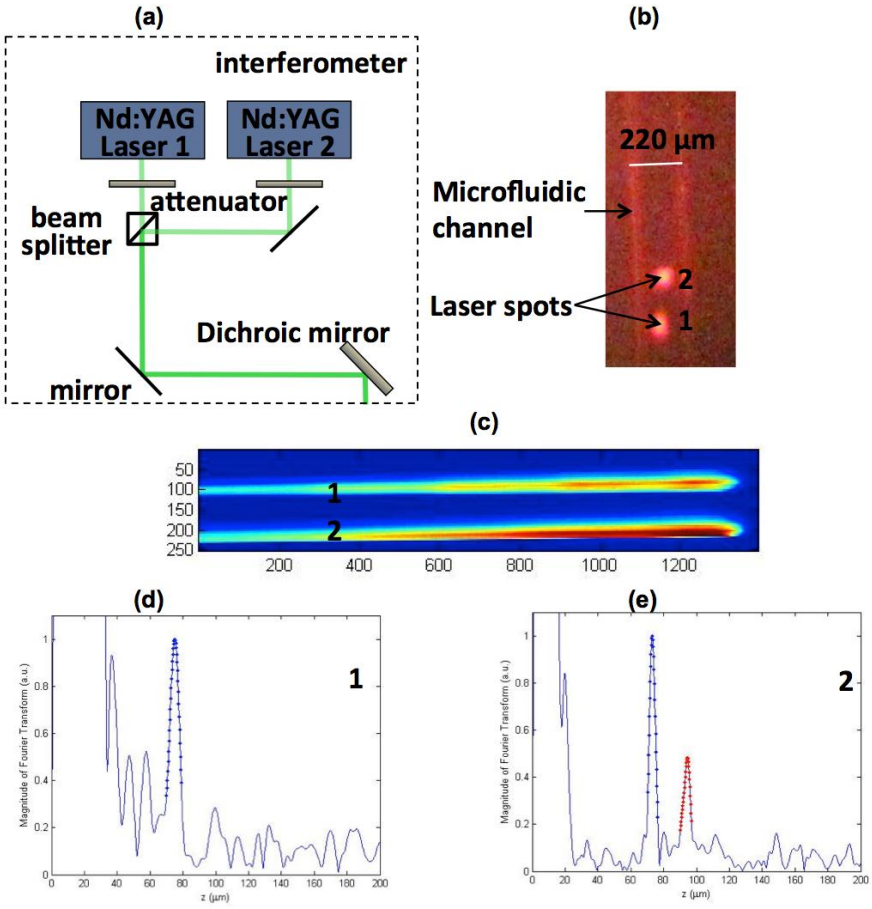


**Figure 5-4: (a) Schematic of the illumination path for the two laser experimental configuration. (b) The two beams, "1" and "2", are aligned vertically along the length of the microfluidic channel with a separation of 220 µm from their centers. (c) Demonstrates simultaneous detection of fluorescence interference from two interrogated particles labeled "1" and "2" corresponding to the laser spots "1" and "2" in (b), respectively. (d-e) Fourier transformed interferometric fringes from spectra "1" and "2" in (c). (d) Reveals only one peak fitted with blue markers indicating that the fluorescent particle was flowing on the surface of the tape. The peak was measured to be at 74.8 ± 2.3 µm. (e) The second particle was located at 94.2 ± 2.3 µm away from the mirror with a tape thickness of 73.1 ± 2.3 µm.**

This experiment used two laser sources to demonstrate proof of concept for line-field imaging capabilities by exhibiting the ability for parallelism in the measurement technique. However, it was limited to detecting self-interference fringes from only two lateral locations (two spots in line) in the microfluidic channel. To overcome this limitation line-field imaging would have to be implemented with a more powerful laser capable of delivering sufficient light intensity throughout the line. In addition, the ideal case would be to change the orientation of the channel from a vertical position to a horizontal one. This would avoid the need to rotate the detection path optics and allow the spectra arising from particles flowing next to each other to be separated out vertically on the CCD.

## 5.5. Summary

This chapter presented the experimental results using FCT on the optofluidic sample. In the context of the optofluidic device, the microfluidic channel was used for flowing microspheres through the FCT acquisition system. Two experiments were conducted, one with a single laser source and the other with two laser sources. The second experiment was conducted to demonstrate line field imaging capabilities. The next chapter concludes the thesis, and proposes possible avenues for future work.

# Chapter 6. Conclusions

## 6.1. Summary

The concepts developed through this thesis work established a technical foundation for the combination of Fluorescence Coherence Tomography with microfluidics to open up new possibilities for biological investigations in optofluidics.

The optical system used to demonstrate fluorescence coherence self-interferometry consisted of a common-path interferometer and a custom built spectrometer. The first set of experimental results showed reasonable agreement between measured values and the manufacturer provided thickness values of transparent double sided taped. The double sided tape was used to fabricate the optofluidic sample by adhering the 28 μm tall PDMS microfluidic channel to a gold coated microscope slide that acted as the reference mirror for the FCT signal. Fluorescent microspheres with a diameter of 6 μm were then injected into the channel. The optical system was then used to perform FCT on these flowing fluorescent microspheres. The results showed that the system was able to resolve the axial position of the flowing particle in the microfluidic channel to within the coherence length. Finally, a second excitation laser was introduced to prove the ability for parallelism in the measurement technique and demonstrate proof of concept for line-field imaging capabilities.

The localization of a cell in a microchannel has recently been demonstrated to be highly sensitive to the cell's size and stiffness, which in turn is an important biomarker for cell classification [8]. Wu et al used this concept to differentiate live cells in a mixture containing live and fixed (dead) HeLa cells. In the same report, they also demonstrated the ability to distinguish red blood cells from white blood cells with their optofluidic Lab-on-a-chip device [8]. This thesis demonstrates that FCT would be able to do this for fluorescently labeled cells

The combination of optics with microfluidics allows acquisition of volumetric data, where the flowing particles replace the need for scanning and paves the way to imaging more complex organisms. For example imaging fluorescently labeled *C. elegans*, to demonstrate high resolution functional imaging in scattering media with molecular specificity [35]. The ultimate consequence of these efforts would pave the way for replacing the need for z-stacks in confocal laser scanning microscopy given that FCT acquires axial information simultaneously [36].

To accomplish the long term goal of this thesis which is to open up new possibilities for biological applications in optofluidics, a few challenges would have to be overcome. The challenges are discussed in the following section on future work.

## 6.2. Future work

Before undertaking biological investigations, the challenge of detecting a sufficiently strong self-interference signal from biological specimens with the appropriate cell safe laser power levels has to be addressed (discussed in detail in Chapter 5). To avoid increasing the laser power and causing potential photo damage to cells, this challenge has traditionally been overcome by increasing the exposure (integration time) of the detector to gather more photons at each pixel. However in the case of FCT optofluidics, increasing the exposure decreases the flow rate which consequently decreases the throughput of particles in the microfluidic device; a potential major drawback for optofluidic applications. In addition, another undesirable affect of increasing the integration time of the detector is the increase of thermal noise (dark current) from the CCD chip temperature. However, this can be overcome by cooling the CCD to a temperature at which dark current is insignificant for a certain exposure interval [51]. Alternatively, a fast-gated intensified CCD (ICCD), or similar high sensitivity – low noise detector, could be used that performs very well in extremely low light conditions [52]. This would be ideal because it would permit exposure reduction and CCD gain increase (is shown to be shot-noise limited) resulting in higher particle throughput in FCT optofluidic applications. Another example of a suitable detector is an electron multiplying CCD (EMCCD) which is usually deep cooled (<-70$^{o}$C), has a high quantum efficiency response/conversion in the visible range, and has a relatively fast

frame rate but still limited to millisecond time scales (and longer) [52], [53]. By replacing the current detector with an ICCD, EMCCD, or a cooled CCD, the SNR would improve significantly. A significant drawback of these detectors is that they are very expensive in relation to consumer grade detectors (on the order of a factor of 10).

A related challenge is that the detector suffered from prominent aberrations such as spherical, coma, and astigmatism. The aberrations reduced SNR by warping the fringes on the detector resulting in a blurred averaged interferometric spectrum. To address this issue, one option would be to use higher quality optics designed specifically to compensate for aberrations. Alternatively, this issue could be addressed in the post processing stage of images by applying dewarping techniques to compensate for the distortions in the interferometric fringes. Replacing the detector for a more sensitive one and incorporating new optics would be necessary for biological applications.

Having demonstrated parallel acquisition with FCT using two laser spots, future work could extent to implementing a proper line field excitation scheme capable of interrogating the width of the microfluidic channel. This could be achieved by using a more powerful laser (≥ 100 mW), capable of delivering sufficient light intensity throughout the line. In order to maintain uniformity in laser exposure intensity across the channel, beam shaping optics should also be applied for generating a ‘top-hat’ profile along the laser line.

Beyond simple optics, detector changes, and new post processing techniques, the focus of future work should be to transfer the FCT technology from its current “bulky” state to a compact or on-chip implementation. Currently, FCT is a ‘bulky optical imaging’ technique for microfluidics [16] as the focus of this thesis was to demonstrate that self-interference fluorescence is achievable and compatible with microfluidics. However, for compact or on-chip imaging technique, self-interference fluorescence will be challenging. Nonetheless to benefit from the full potential of this technology as a portable hand-held device for point of care applications, the interferometer and spectrometer need to have a compact or on-chip implementation.

In conclusion, based on the feasibility provided by this thesis and with these future improvements, FCT optofluidics has the potential to provide researchers and scientists with a new significant biological imaging technique.

# References


[1] K. R. Calvo, C. S. McCoy, and M. Stetler-Stevenson, “Flow cytometry immunophenotyping of hematolymphoid neoplasia.,” *Methods Mol. Biol.*, vol. 699, pp. 295–316, Jan. 2011.

[2] R. Frita, M. Rebelo, A. Pamplona, A. M. Vigario, M. M. Mota, M. P. Grobusch, and T. Hänscheid, “Simple flow cytometric detection of haemozoin containing leukocytes and erythrocytes for research on diagnosis, immunology and drug sensitivity testing.,” *Malar. J.*, vol. 10, no. 1, p. 74, Jan. 2011.

[3] V. Wongchotigul, N. Suwanna, S. Krudsood, D. Chindanond, S. Kano, N. Hanaoka, Y. Akai, Y. Maekawa, S. Nakayama, S. Kojima, and S. Looareesuwan, “The use of flow cytometry as a diagnostic test for malaria parasites.,” *Southeast Asian J. Trop. Med. Public Health*, vol. 35, no. 3, pp. 552–9, Sep. 2004.

[4] X. Mao, A. Nawaz, S. Lin, and M. Lapsley, “An integrated, multiparametric flow cytometry chip using ‘microfluidic drifting’ based three-dimensional hydrodynamic focusing,” *Biomicrofluidics*, vol. 024113, 2012.

[5] C. Chang, Z. Huang, and R. Yang, “Three-dimensional hydrodynamic focusing in two-layer polydimethylsiloxane (PDMS) microchannels,” *J. Micromechanics Microengineering*, vol. 17, 2007.

[6] N. Sundararajan, M. Pio, L. P. Lee, and A. A. Berlin, “Three-dimensional hydrodynamic focusing in polydimethylsiloxane (PDMS) microchannels,” *J. Microelectromechanical Syst.*, vol. 13, no. 4, pp. 559–567, 2004.

[7] S. Lin, P. Yen, C. Peng, and Y. Tung, “Single channel layer, single sheath-flow inlet microfluidic flow cytometer with three-dimensional hydrodynamic focusing,” *Lab Chip*, pp. 3135–3141, 2012.

[8] T.-F. Wu, Z. Mei, and Y.-H. Lo, “Optofluidic device for label-free cell classification from whole blood.,” *Lab Chip*, vol. 12, no. 19, pp. 3791–7, Oct. 2012.

[9] S. Yu, J. Zhang, M. S. Moran, J. Q. Lu, Y. Feng, and X. Hu, “A novel method of diffraction imaging flow cytometry for sizing microspheres,” *Cytometry*, vol. 20, no. 20, pp. 22245–22251, 2012.

[10] G. M. Whitesides, “The origins and the future of microfluidics.,” *Nature*, vol. 442, no. 7101, pp. 368–73, Jul. 2006.

[11] J. Wu and M. Gu, “Microfluidic sensing: state of the art fabrication and detection techniques.,” *J. Biomed. Opt.*, vol. 16, no. 8, p. 080901, Aug. 2011.

[12] K. M. Jacobs, J. Q. Lu, and X. Hu, “Development of a diffraction imaging flow cytometer,” *Opt. Lett.*, vol. 34, no. 19, pp. 2985–2987, 2009.

[13] K. Jacobs, L. Yang, J. Ding, A. E. Ekpenyong, R. Castellone, J. Q. Lu, and X.-H. Hu, “Diffraction imaging of spheres and melanoma cells with a microscope objective,” *J. Biophotonics*, pp. 521–527, 2009.

[14] D. Barat, G. Benazzi, M. C. Mowlem, J. M. Ruano, and H. Morgan, “Design, simulation and characterisation of integrated optics for a microfabricated flow cytometer,” *Opt. Commun.*, vol. 283, no. 9, pp. 1987–1992, May 2010.

[15] J. Godin, C. Chen, S. Cho, W. Qiao, F. Tsai, and Y.-H. Lo, “Microfluidics and photonics for Bio-System-on-a-• Chip: A review of advancements in technology towards a microfluidic flow cytometry chip,” *J. Biophotonics*, vol. 376, no. 5, pp. 355–376, 2008.

[16] J. Wu, G. Zheng, and L. M. Lee, “Optical imaging techniques in microfluidics and their applications.,” *Lab Chip*, vol. 12, no. 19, pp. 3566–75, Oct. 2012.

[17] D. Psaltis, S. R. Quake, and C. Yang, “Developing optofluidic technology through the fusion of microfluidics and optics.,” *Nature*, vol. 442, no. 7101, pp. 381–6, Jul. 2006.

[18] D. A. Boas, C. Pitris, and N. Ramanujam, *Handbook of Biomedical Optics*, vol. 11, no. 1. CRC Press, 2011, p. 787.

[19] L. V. Wang and H. Wu, *Biomedical Optics: Principles and Imaging*. John Wiley & Sons, 2007, p. 362.

[20] A. F. Fercher, W. Drexler, C. K. Hitzenberger, and T. Lasser, “Optical coherence tomography - principles and applications,” *Reports Prog. Phys.*, vol. 66, no. 2, pp. 239–303, 2003.

[21] K. H. Drexhage, “IV interaction of light with monomolecular dye layers,” in in *Progress in Optics*, E.Wolf, Ed. Elsevier, 1974, pp. 163–232.

[22] R. R. Chance, A. Prock, and R. Silbey, “Molecular Fluorescence and Energy Transfer Near Interfaces,” in in *Advances in Chemical Physics*, Wiley, 1978, pp. 1–65.

[23] K. E. Drabe, G. Cnossen, and D. A. Wiersma, “Localization of pontaneous emission in front of a mirror,” *Opt. Commun.*, vol. 73, no. 2, pp. 91–95, 1989.

[24] A. Lambacher and P. Fromherz, “Fluorescence interference-contrast microscopy on oxidized silicon using a monomolecular dye layer,” *Appl. Phys. A 63*, pp. 207–216, 1996.

[25] D. Braun and P. Fromherz, “Invited paper Fluorescence interference-contrast microscopy of cell adhesion on oxidized silicon,” *Appl. Phys. A 65*, pp. 341–348, 1997.

[26] A. Lambacher and P. Fromherz, “Luminescence of dye molecules on oxidized silicon and fluorescence interference contrast microscopy of biomembranes,” *J. Opt. Soc. Am. B*, vol. 19, no. 6, p. 1435, Jun. 2002.

[27] P. V Ganesan and S. G. Boxer, “A membrane interferometer.,” *Proc. Natl. Acad. Sci. U. S. A.*, vol. 106, no. 14, pp. 5627–32, Apr. 2009.

[28] A. K. Swan, L. A. Moiseev, C. R. Cantor, B. Davis, S. B. Ippolito, W. C. Karl, B. B. Goldberg, M. S. Ünlü, and S. Member, “Toward Nanometer-Scale Resolution in Fluorescence Microscopy Using Spectral Self-Interference,” *Quantum*, vol. 9, no. 2, pp. 294–300, 2003.

[29] L. Moiseev, C. R. Cantor, M. I. Aksun, M. Dogan, B. B. Goldberg, a. K. Swan, and M. S. Ünlü, “Spectral self-interference fluorescence microscopy,” *J. Appl. Phys.*, vol. 96, no. 9, p. 5311, 2004.

[30] L. Moiseev, M. S. Ünlü, A. K. Swan, B. B. Goldberg, and C. R. Cantor, “DNA conformation on surfaces measured by fluorescence self-interference,” *Proc. Natl. Acad. Sci. U. S. A.*, vol. 103, no. 8, pp. 2623–2628, 2006.

[31] B. J. Davis, A. K. Swan, M. S. Unlü, W. C. Karl, B. B. Goldberg, J. C. Schotland, and P. S. Carney, “Spectral self-interference microscopy for low-signal nanoscale axial imaging.,” *J. Opt. Soc. Am. A. Opt. Image Sci. Vis.*, vol. 24, no. 11, pp. 3587–99, Nov. 2007.

[32] S. Member, S. Jain, M. B. Goldberg, B. B. Goldberg, A. K. Swan, S. Member, and M. S. Unl, “Spectral Self-Interference Fluorescence Microscopy for Subcellular Imaging,” *Quantum*, vol. 14, no. 1, pp. 217–225, 2008.

[33] A. Bilenca, A. Ozcan, B. Bouma, and G. Tearney, “Fluorescence coherence tomography.,” *Opt. Express*, vol. 14, no. 16, pp. 7134–43, Aug. 2006.

[34] A. St Quintin, L.-K. Merhi, and M. V Sarunic, “Spectral domain fluorescence coherence phase microscopy.,” *Appl. Opt.*, vol. 50, no. 12, pp. 1798–804, Apr. 2011.

[35] S. Pang, X. Cui, J. DeModena, Y. M. Wang, P. Sternberg, and C. Yang, “Implementation of a color-capable optofluidic microscope on a RGB CMOS color sensor chip substrate.,” *Lab Chip*, vol. 10, no. 4, pp. 411–4, Feb. 2010.

[36] A. Bilenca, T. Lasser, A. Ozcan, R. a Leitgeb, B. E. Bouma, and G. J. Tearney, “Image formation in fluorescence coherence-gated imaging through scattering media.,” *Opt. Express*, vol. 15, no. 6, pp. 2810–21, Mar. 2007.

[37] A. St Quintin, “Spectral domain fluorescence coherence phase microscopy,” Simon Fraser University, 2010.

[38] W. Drexler and J. G. Fujimoto, Eds., *Optical Coherence Tomography*. Berlin, Heidelberg: Springer Berlin Heidelberg, 2008.

[39] M. Choma, M. Sarunic, C. Yang, and J. Izatt, “Sensitivity advantage of swept source and Fourier domain optical coherence tomography.,” *Opt. Express*, vol. 11, no. 18, pp. 2183–9, Sep. 2003.

[40] L. S. Pedrotti and F. L. Pedrotti, “Laser Beam Characteristics,” in in *Introduction to Optics*, 2nd ed., Englewood Cliffs, N.J: Prentice Hall, 1993, pp. 457–479.

[41] A. F. T. Von M. Czerny, “Uber den Astigmatismus bei Spiegelspektrometern.,” *Zeitschrift für Phys. A Hadron. Nucl.*, no. 61, pp. 792–797, 1930.

[42] F. L. Pedrotti and L. S. Pedrotti, “The Diffraction Grating,” in in *Intoduction to Optics*, 2nd ed., Englewood Cliffs, N.J: Prentice Hall, 1993, pp. 352–353.

[43] P. a Aarts, P. a Bolhuis, K. S. Sakariassen, R. M. Heethaar, and J. J. Sixma, “Red blood cell size is important for adherence of blood platelets to artery subendothelium.,” *Blood*, vol. 62, no. 1, pp. 214–7, Jul. 1983.

[44] S. D. G. Thermo Scientific, “Red Fluorescent Microspheres.” [Online]. Available: http://distrilabparticles.com/library/uploads/documenten/Red_fluorescent_microspheres.pdf.

[45] “Thorlabs - Protected Gold Mirrors.” [Online]. Available: http://www.thorlabs.com/newgrouppage9.cfm?objectgroup_id=744.

[46] “Thorlabs - Optically Clear Double-Sided Adhesive Tape.” [Online]. Available: http://www.thorlabs.de/newgrouppage9.cfm?objectgroup_id=4973.

[47] C. S. Thompson and A. R. Abate, “Electronic Supplementary Information (ESI)-Adhesive-based bonding technique for PDMS microfluidic devices,” *Lab Chip*, p. 40978, 2013.

[48] Y. Xia and G. M. Whitesides, “Soft lithography,” no. 12, 1998.

[49] C. S. Thompson and A. R. Abate, “Adhesive-based bonding technique for PDMS microfluidic devices.,” *Lab Chip*, vol. 13, no. 4, pp. 632–5, Feb. 2013.

[50] A. van O. Peter Hinterdorfer, *Handbook of Single-Molecule Biophysics*. 2009.

[51] T. J. Fellers, K. M. Vogt, and M. W. Davidson, “Nikon MicroscopyU | Interactive Java Tutorials | CCD Signal-To-Noise Ratio,” 2013. [Online]. Available: http://www.microscopyu.com/tutorials/java/digitalimaging/signaltonoise/.

[52] D. Dussault and P. Hoess, “Noise performance comparison of ICCD with CCD and EMCCD cameras,” in *Optical Science and Technology, the SPIE 49th Annual Meeting*, 2004, pp. 195–204.

[53] “Nikon MicroscopyU | Optical System and Detector Requirements for Live-Cell Imaging,” 2013. [Online]. Available: http://www.microscopyu.com/articles/livecellimaging/imagingsystems.html.

# Appendix A

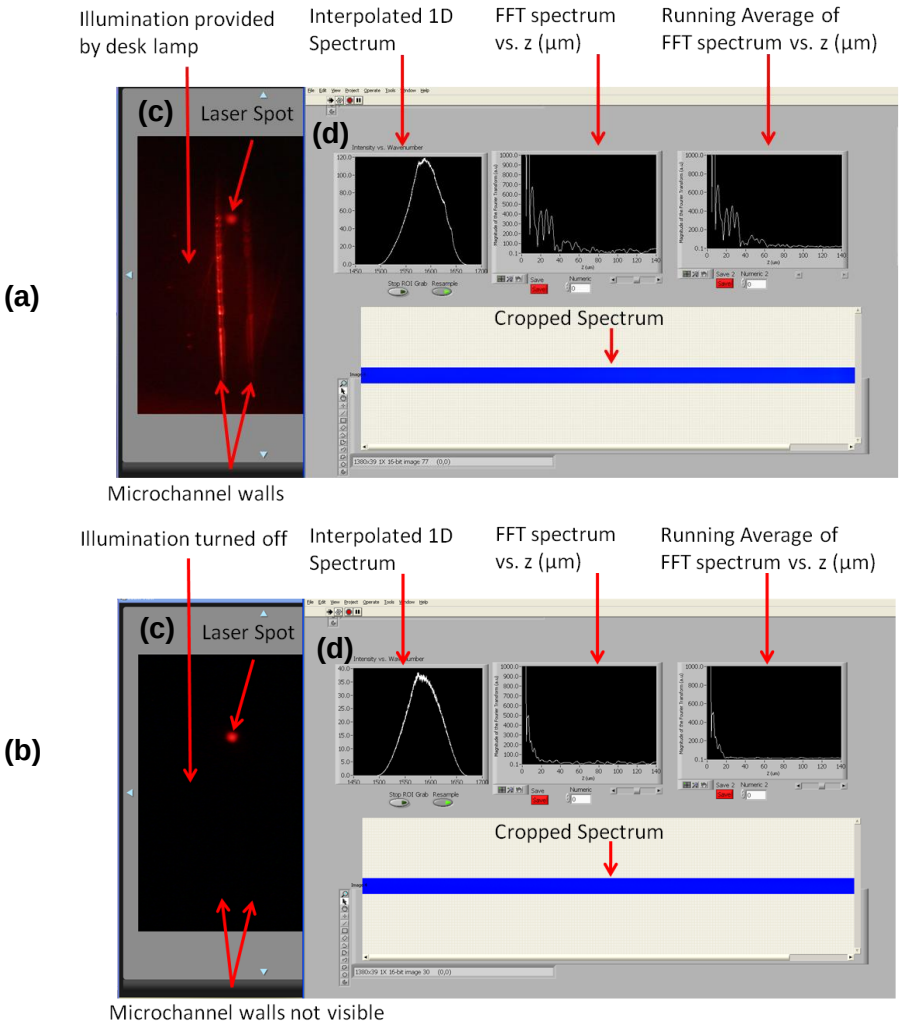


**Figure 6-1: (a) Desk lamp used for side illumination of microfluidic channel. (b) desk lamp turned off. (c) Screen capture of live view mode of Canon EOS utility program and (d) custom built Labview acquisition program.**